ADVANCES IN THE SCIENCE AND TECHNOLOGY OF DIESEL PARTICULATE FILTER SIMULATION

Athanasios G. Konstandopoulos[1,2,*], Margaritis Kostoglou[1,3], Nickolas Vlachos[1] and Evdoxia Kladopoulou[1]

[1]**Aerosol & Particle Technology Laboratory, CERTH/CPERI, P.O. Box 361, Thermi Thessaloniki 57001, Greece**

[2]**Department of Chemical Engineering, Aristotle University, P.O. Box 1517, 54006, Thessaloniki, Greece**

[3]**Division of Chemical Technology, Department of Chemistry, Aristotle University, Univ. Box 116, 541 24 Thessaloniki, Greece**

*Corresponding author. Tel.: + 30 2310 498192; Fax: + 30 2310 498190.
E-mail: agk@cperi.certh.gr

Advances in Chemical Engineering, vol. 33
ISSN 0065-2377
DOI 10.1016/S0065-2377(07)33004-4

Abstract

As diesel emissions regulations are becoming more stringent, diesel particulate filters (DPFs) have become possibly the most important and complex diesel emission control device. A traditional design of experiments approach becomes very time consuming and costly if one wants to address DPF design, system integration, regeneration control strategy optimization and ash ageing assessment, due to the very large number of tests needed. The application of simulation tools provides a promising alternative and hence simulation is increasingly being used for the design of exhaust emission control systems. In a DPF many coupled physico-chemical phenomena occur over widely disparate spatial and temporal scales and the simulation approach should account for and exploit these features. This becomes possible with the introduction of certain defensible assumptions and/or simplifications to arrive at an accurate but computationally tractable DPF simulation approach, for the needs of industrial users. The present chapter summarizes the current state of the science and technology of DPF simulation, from the Aerosol & Particle Technology Laboratory (APTL), addressing consistent and rigorous refinements in a number of areas including: the aerodynamics at the filter and channel inlet, flow, filtration and reaction phenomena at the DPF material microstructure scale, and in coupling/interfacing DPF simulation with three-dimensional (3D) Computational Fluid Dynamics (CFD) codes. Experimental results are cited where appropriate, to re-enforce/validate the points brought forward by the simulation approach.

I. Introduction

Advanced fuel injection technology in conjunction with an inherent high thermal efficiency have lead to increased market share of diesel powered vehicles especially in Europe, where the modern diesel passenger car is increasingly perceived by consumers, as an environmentally friendly and cost-effective transport means. This increasing market penetration of the diesel powertrain is expected to continue, if the diesel engine is able to meet even more stringent emission limits in the future. The first successful market introduction of vehicles equipped with diesel particulate filters (DPFs) and fuel-borne catalyst assisted regeneration took place in 2001 (Blanchard *et al.*, 2004) and since then DPFs have become possibly the most important and complex diesel emission control device. The deployment of DPFs is also necessary for complying with heavy-duty engine emission standards while retrofit applications of passive DPF systems for heavy-duty vehicles are already widespread during the last decade.

Recent developments (Bardon *et al.*, 2004; Boretto *et al.*, 2004; Ogyu *et al.*, 2004; Young *et al.*, 2004) in passenger car emission control systems are focusing on so-called "fit-for-life" solutions, eliminating the servicing of the DPF (ash removal) during the vehicle's lifetime. Durability of the engine and emission control system is also very important in heavy-duty vehicles. Consequently, the emission control engineer must find practical and cost-effective solutions, which in addition to particulate emission reduction should not hamper the also challenging task of reduction of nitrogen oxide (NO_x) emissions.

NO_x reduction has relied up to now predominantly on advanced in-cylinder reduction (exhaust gas recirculation, new combustion concepts) approaches, but aftertreatment technologies such as lean NO_x traps (LNT) and lean NO_x converters (LNC) are actively researched for passenger car application, while urea-based selective catalytic reduction (SCR) systems have already been introduced in the heavy-duty market in Europe (Johnson, 2004). Next-generation diesel emission control systems will be complex assemblies of chemical reactors and separators (Fig. 1) sometimes integrating different functionalities on the same monolithic support to achieve demanding requirements in space and cost, especially in passenger cars (Nakatani *et al.*, 2002). Such complex emission control systems require for their cost-effective, design, development, system-level integration and optimization advanced simulation tools. In addition, requirements for robust on-board monitoring and control generate the need for efficient algorithms, implementable in computationally limited engine control units (ECUs), which will provide accurate knowledge of the state of emission control system during vehicle operation, and which can be used in control loops for the management of the integrated powertrain-emission control system.

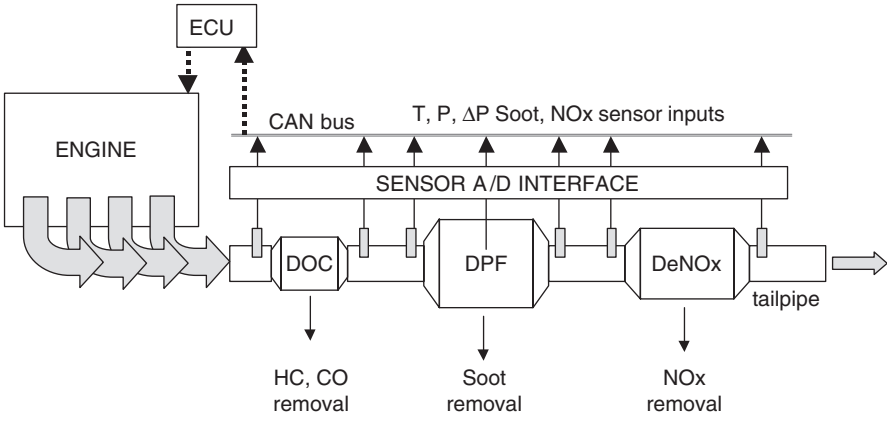

FIG. 1. An example of a future integrated soot-NO_x emission control system. DPF stands for diesel particulate filter. Sensory inputs of temperature (T), pressure (P), pressure drop (ΔP), soot and NO_x concentration will be required along the exhaust pipe.

The aim of the present work is to review some recent advances in DPF simulation science and technology from the Aerosol & Particle Technology Laboratory (APTL). While our current focus is on DPFs some of the mathematical/computational methods (especially those related to porous media and microstructures) may be applicable in other catalytic converter systems. Advances in DPF simulation are presented according to a taxonomy based on different spatial scales, originally introduced from this laboratory in Konstandopoulos and Kostoglou (1999a) and exploited in Konstandopoulos and Kostoglou (1999b, 2000, 2004), Konstandopoulos *et al.* (2000, 2001, 2003) and Kostoglou *et al.* (2003) to build hierarchically a state-of-the-art DPF simulation approach. Experimental results are cited where appropriate, to re-enforce/validate the points brought forward by the simulation approach.

II. The Many Scales of DPF Systems

The multiscale nature of DPFs has been already addressed in Konstandopoulos and Kostoglou (1999b, 2000, 2004), Konstandopoulos *et al.* (2000, 2001, 2003) and Kostoglou *et al.*, 2003, and spans several orders of magnitude, as shown in Fig. 2.

This multitude of scales provides a useful way to organize a "divide-and-conquer strategy" for the simulation of DPFs, with typical examples given in Konstandopoulos and Kostoglou (1999b); Konstandopoulos *et al.* (2001, 2003), Bissett (1984) and Bissett and Shadman (1985). Generally, there are three simultaneous length scales that need to be considered for the modeling of DPFs. The first one refers to the phenomena occurring across the soot layer and the porous filter walls, the second one to the phenomena occurring along the filter channels and the third one is the macroscopic scale of the entire DPF. Recent developments from our work at each scale are presented in the following sections.

III. Filter Wall Scale

This section summarizes the advances in the description of flow, transport and reaction phenomena in the filter wall scale. The filter wall scale is the one which triggers the material development in the field: new filter structures, multifunctional catalyst coatings and ash interactions (SAE International, 2004). In addition, at this scale the structural aspects of the deposited soot particles need to be considered.

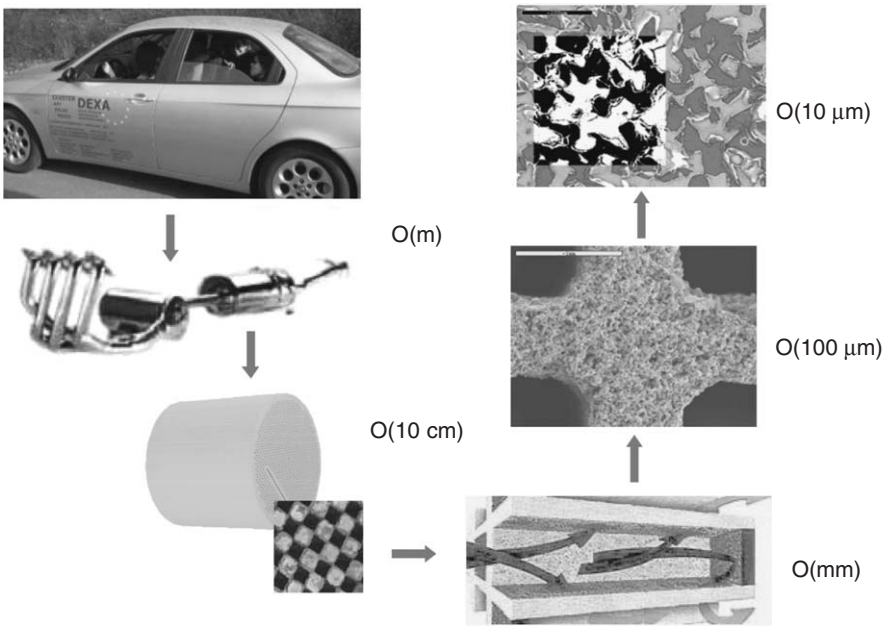

FIG. 2. DPF simulation has to face multiple scales. Figure from Konstandopoulos and Kostoglou (2004).

A. Classic Flow in Porous Media Descriptors

Flow resistance descriptors of DPF walls, experimental protocols for their determination and useful correlations have been previously presented in Konstandopoulos (2003). At the filter wall scale flow resistance is determined by the Darcy permeability k and the Forchheimer coefficient β of the wall.

$$\Delta P_{\text{wall}} = \underbrace{\frac{\mu}{k} u_{\text{w}} w_{\text{s}}}_{\text{Darcy}} + \underbrace{\beta \rho u_{\text{w}}^2 w_{\text{s}}}_{\text{Forchheimer}} \tag{1}$$

A general correlation extending over five orders of magnitude for the permeability of porous DPF walls made of extruded, sintered "grains" was given in Konstandopoulos (2003), which can be expressed as:

$$k_{\text{wall}} = f_{\text{w}}(\varepsilon) \cdot d_{\text{c}}^2 \cdot \text{SCF}(d_{\text{c}}) \tag{2}$$

where SCF is a factor accounting for slip-flow and free molecular effects (based on the prevailing mean free path and the grain diameter d_{c} of typical filter

media), and the function $f_w(\varepsilon)$ was given in several equivalent forms (Konstandopoulos, 2003).

It was also suggested in Konstandopoulos (2003) and Konstandopoulos *et al.* (2001) that the Forchheimer coefficient β and the Darcy permeability k were interconnected in accordance with:

$$\beta = \frac{\text{constant}}{\varepsilon^{1.5}\sqrt{k}} \tag{3}$$

The value of the constant in Eq. (3) depends on the actual morphology of the elements making up the porous medium and it was estimated for beds of spheres as 0.143, based on the original Ergun's correlation or as 0.134 for smooth and 0.298 for rough particles of packed beds, based on newer compilations (Dullien, 1979). The Forchheimer contribution to the pressure drop is negligible unless filters are operated at relatively high filtration velocities, which can occur for some filter designs based on sheets of sintered metal materials. Experiments performed with granular sintered metal filter media (Konstandopoulos *et al.*, 2005) have shown that Eq. (3) can be applicable with a value of the constant equal to 0.34 (Fig. 3). This is in good agreement with the value of 0.3 mentioned in Konstandopoulos (2003), Konstandopoulos *et al.* (2001) by analogy to macroscopic rough granular media (Dullien, 1979).

Equation (3) is also applicable for fibrous filter media (Fig. 4) with the constant being 16.6. The scatter observed can be attributed to the fact that the porosity of fibrous filters shows higher local inhomogeneity, meaning that the variations of each sample to the nominal specified porosity are likely to be higher.

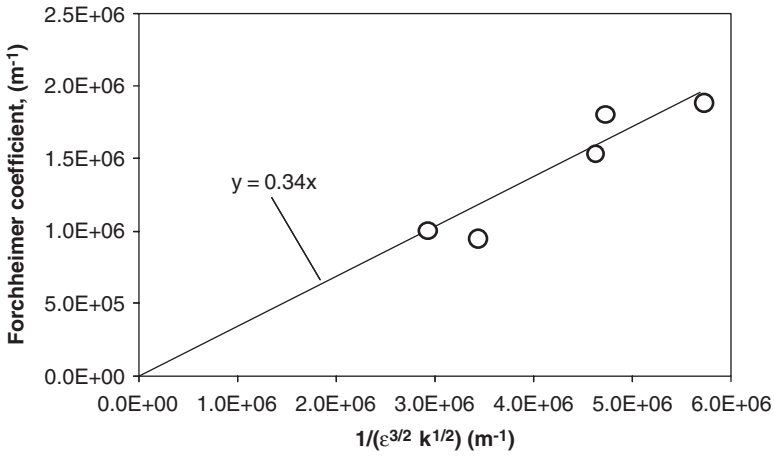

FIG. 3. Validity of Eq. (3) for sintered metal granular filters.

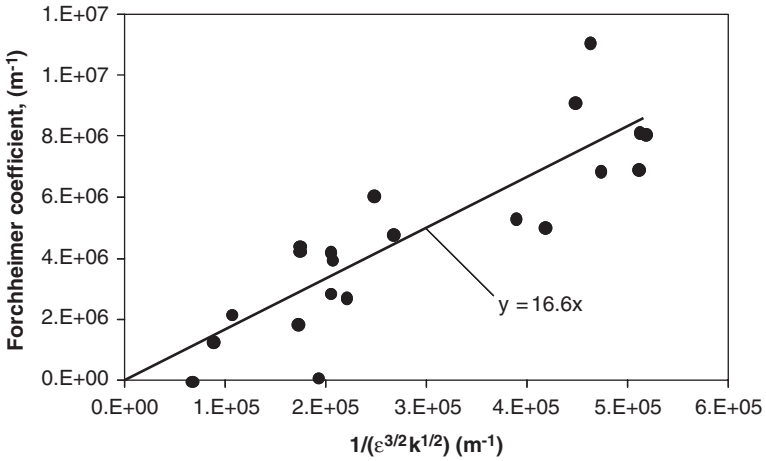

FIG. 4. Validity of Eq. (3) for fibrous filters.

B. MICROFLOW SIMULATION TECHNOLOGY

The characterization of the flow in existing DPF materials has been assessed by experiments and macroscopic continuum flow in porous media approaches. However, when it comes to material design it is essential to employ flow simulation techniques in geometrically realistic representations of DPF porous media. Some first applications were introduced in Konstandopoulos (2003) and Muntean *et al*. (2003) and this line of research is especially important for the development of new filter materials, the optimization of catalyst deposition inside the porous wall and for the design of gradient-functional filter microstructures where multiple functionalities in terms of particle separation and catalyst distribution (for combined gas and particle emission control) can be exploited.

Using advances in computer reconstruction methods (see e.g. Kikkinides and Burganos, 2000; Torquato, 2001) and past experience with discrete particle deposit simulations (Konstandopoulos, 2000), we have developed algorithmic as well as process-based reconstruction techniques to generate three-dimensional (3D) "digital materials" that are faithful representations of DPF microstructures. We refer to this approach as DPF microflow simulation (MicroFlowS). MicroFlowS is thus a short name for a computational approach, which combines

(i) Statistical methods and descriptors (see e.g. Kikkinides and Burganos, 2000; Torquato, 2001) to characterize the microstructure of DPF porous materials (bare as well as coated).
(ii) Computer reconstruction algorithms for the realistic representation of DPF porous media and particle deposit microstructures (see e.g.

Kikkinides and Burganos, 2000; Konstandopoulos, 2000; Tassopoulos, 1991; Tomadakis and Sotirchos, 1991a, b; Torquato, 2001).

(iii) Fluid flow and particle transport, deposition and reaction algorithms in the reconstructed porous materials (employing Lattice Boltzmann (LB) techniques, see e.g. Chen and Doolen, 1998).

Examples of computer reconstructed DPF porous media are given in Fig. 5 and encompass all currently available filtration media: extruded ceramic filters (including reaction formed media as cordierite and grain-sintered media as SiC), fibrous filters, foams and sintered metal powder/wiremesh.

A distinctive advantage of having "digital materials" at our disposal is the ability to study catalyst deposition processes in these media. Depending on the way the catalyst is applied (e.g. from a solution or from a slurry) the catalyst coating degree of uniformity (Fig. 6) is expected to lead to different flow resistance behavior of the DPF.

To illustrate the quantitative nature of MicroFlowS, we describe the application of the approach to SiC filter structures with pore sizes in the range

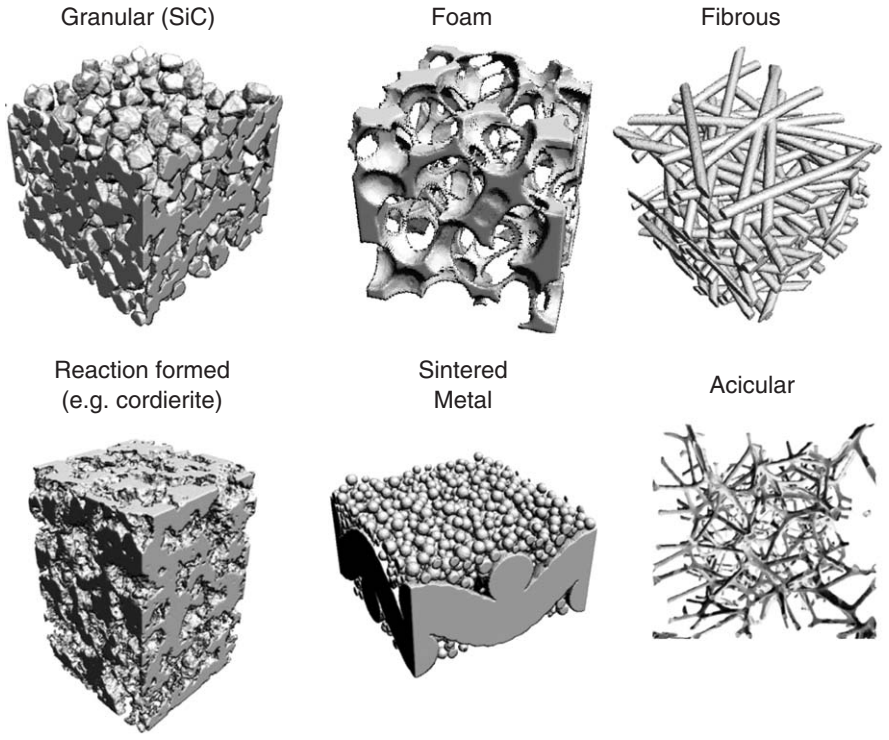

FIG. 5. Computer reconstruction of various porous filter structures.

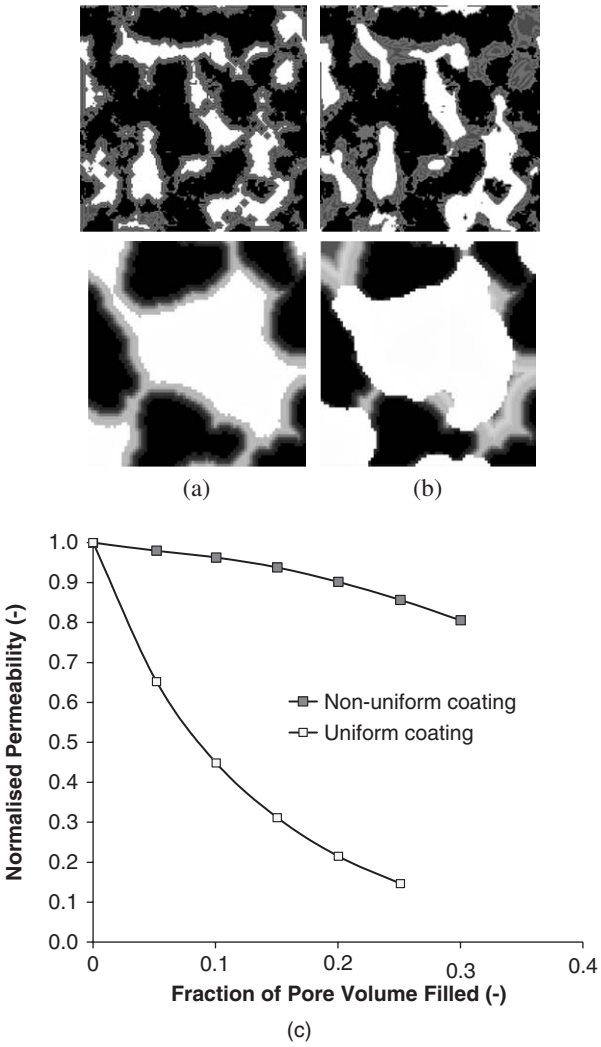

FIG. 6. Simulation of catalytic coating deposition at the same integral quantity of catalyst load. (a) Uniform coating and (b) non-uniform coating. The color code (blue to red) assists to visualize the local catalyst coating thickness from the filter surface. (c) Effect of coating distribution (uniform vs. non-uniform) on the DPF permeability (see Plate 7 in Color Plate Section at the end of this book).

from 10 to 90 μm and porosities in the range of 40–50%. At first scanning electron microscope (SEM) images of the filter wall are taken at different magnifications, as shown in Fig. 7(a) and (b), to identify the range of homogeneity of the material. Then a number of polished cross sections of the material embedded in a special resin are prepared and additional images in the

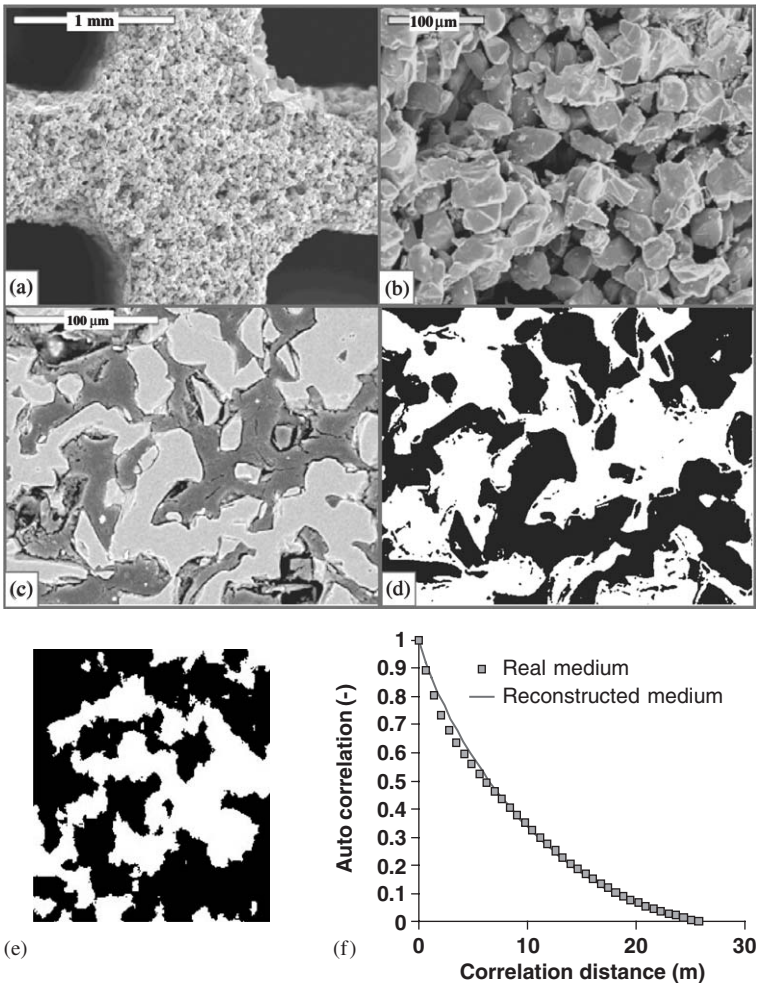

FIG. 7. (a) and (b) SEM images of filter walls, (c) backscattered SEM image of a filter wall, (d) binary thresholded image. The pore space is denoted in black color. (e) Computer reconstruction of filter shown in (d) and (f) Comparison of autocorrelation function of reconstructed medium to that of the real filter.

SEM backscattered image mode are obtained, e.g. Fig. 7(c). The SEM image is converted into a binary image (with appropriate thresholding algorithms) as shown in Fig. 7(d). The binary image is then analyzed with respect to different statistical descriptors (e.g. porosity, autocorrelation function). Subsequently an appropriate reconstruction algorithm is employed (in the particular case as in the method of Kikkinides and Burganos, 2000) producing the reconstructed ''digital material'', shown in Fig. 7(e). The ''real'' and ''reconstructed'' materials

have in a statistical sense the same "porosity" and "pore size", as manifested through the very good agreement of their autocorrelation functions (Kikkinides and Burganos, 2000), shown in Fig. 7(f).

The flow resistance behavior of the reconstructed medium can now be examined by performing 3D flow simulations with the Lattice Boltzmann method (Chen and Doolen, 1998), and obtaining the permeability of the material (Konstandopoulos, 2003). Figure 8(a) depicts a visualization of 3D flow "tubes" and flow velocity distributions at different cross sections in a reconstructed filter material. Figure 8(b) shows the comparison of computer simulated and experimental permeabilities obtained with the experimental protocol described in Konstandopoulos (2003).

C. Soot Deposit Microstructure

In the literature, the assumption that the soot layer grown on the filter wall could be described by a uniform density (equivalently porosity), surface area and permeability has been common practice. These are parameters that had to be tuned according to experiments, leading to widely varying values among different publications, that for the sake of brevity will not be reviewed here. Konstandopoulos *et al.* (2002) demonstrated that during filter loading the microstructure of the soot cake is determined by the convective-diffusive transport of the soot aggregates toward the deposit and it was shown that soot cake packing density (ρ) and permeability (k_{soot}) were related to the local value of the dimensionless mass transfer Peclet number, Pe. Moreover, these parameters can be related to the porosity ε and primary particle size (d_{pr}) of the soot aggregates as follows (Konstandopoulos *et al.*, 2002):

$$\rho = \tilde{\rho} \cdot (1 - \varepsilon) \tag{4}$$

$$k_{\text{soot}} = f(\varepsilon) \cdot d_{\text{pr}}^2 \cdot \text{SCF} \tag{5}$$

where SCF is the Stokes–Cunningham factor calculated with a Knudsen number (Kn) based on the primary soot particle size (d_{pr}) by:

$$\text{SCF} = 1 + Kn \cdot (1.257 + 0.4\text{e}^{-1.1/Kn}) \tag{6}$$

and $f(\varepsilon)$ the Kuwabara function of porosity ε, given as (Konstandopoulos and Johnson, 1989):

$$f(\varepsilon) = \frac{2}{9}\left[\frac{2 - \frac{9}{5}(1-\varepsilon)^{1/3} - \varepsilon - \frac{1}{5}(1-\varepsilon)^2}{(1-\varepsilon)}\right] \tag{7}$$

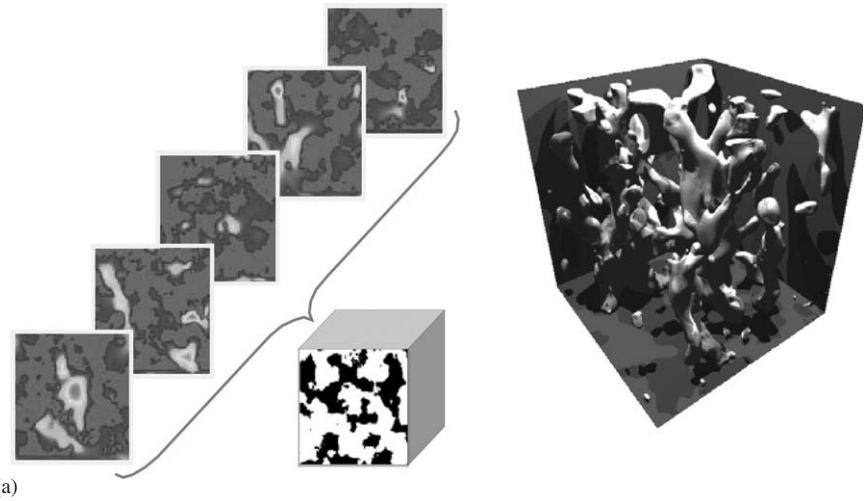

(a)

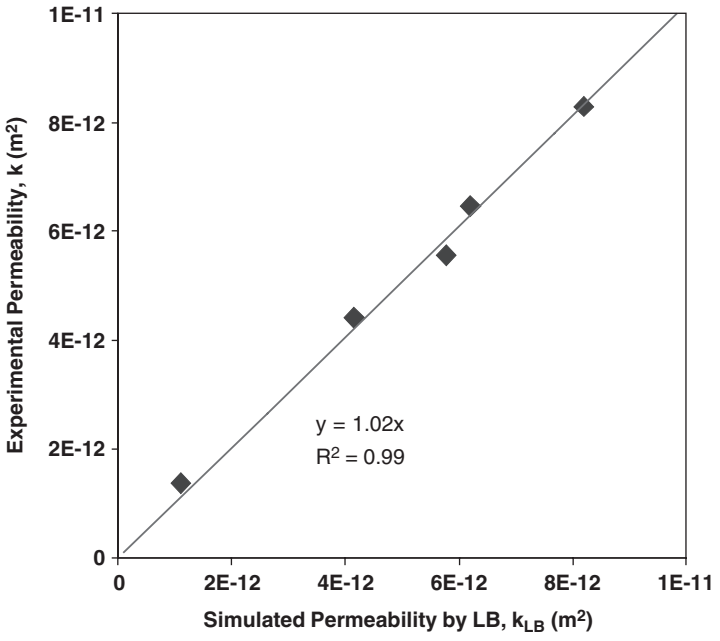

(b)

FIG. 8. (a) Velocity fields at different sections through the reconstructed filter wall (gray denotes the solid material, violet denotes lowest and red denotes highest velocity) and visualization of flow paths in the reconstructed filter wall and (b) comparison of experimental and simulated filter permeabilities (see Plate 8 in Color Plate Section at the end of this book).

These parameters should not therefore be interpreted as constant, intrinsic physical properties of the soot cake, but rather as dynamic properties that depend on the deposit growth mechanism and its history.

Further insight into soot cake properties has been obtained by model experiments with soot aggregates generated by a Combustion Aerosol Standard (CAST) burner (Matter Engineering, Switzerland). The CAST is a quenched diffusion flame gas (propane) burner that allows the stable and controlled generation of soot aggregates over a much larger size range than that found in diesel exhaust. Figure 9 depicts the hydrodynamic resistance factor $(\rho \times k)_{\text{soot}}$ of CAST soot deposited cakes on flat disk-shaped glass-fiber filters as a function of Peclet number and aggregate mobility diameter d_{ag}.

The values of the aggregate mobility diameters shown in Fig. 9 are values measured by the Scanning Mobility Particle Sizer (SMPS). The data are consistent with a scaling relation of the form:

$$(\rho \times k)_{\text{soot}} = \tilde{\rho} \cdot (1 - \varepsilon) \cdot f(\varepsilon) \cdot d_{\text{pr}}^2 \cdot \text{SCF} \tag{8}$$

where the porosity of the deposits follows a power law in terms of the Peclet number (Rodriguez-Perez *et al.*, 2004):

$$\varepsilon(Pe) = 1 - (1 - \varepsilon_\infty) \cdot \left(1 + \frac{Pe_0}{Pe}\right)^{-n} \tag{9}$$

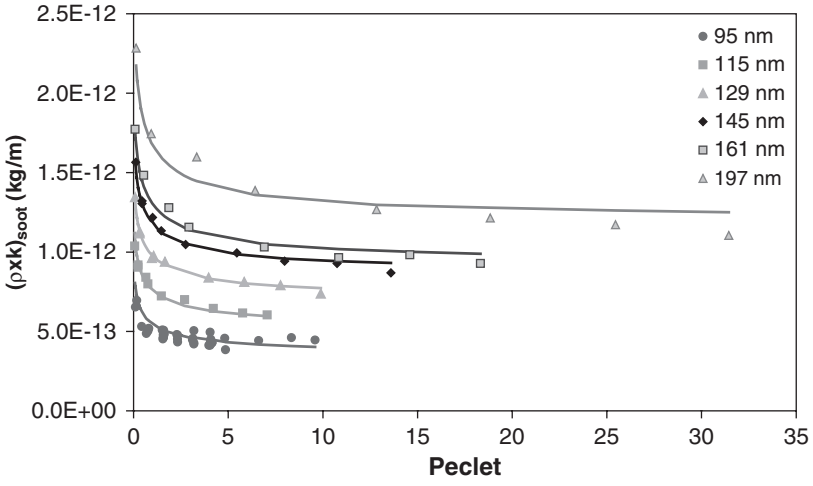

FIG. 9. Experimental measurements of CAST soot hydrodynamic resistance factor as a function of Peclet number and aggregate mobility diameter. The continuous lines are plotted using the scaling relation form Eqs. (8) and (9).

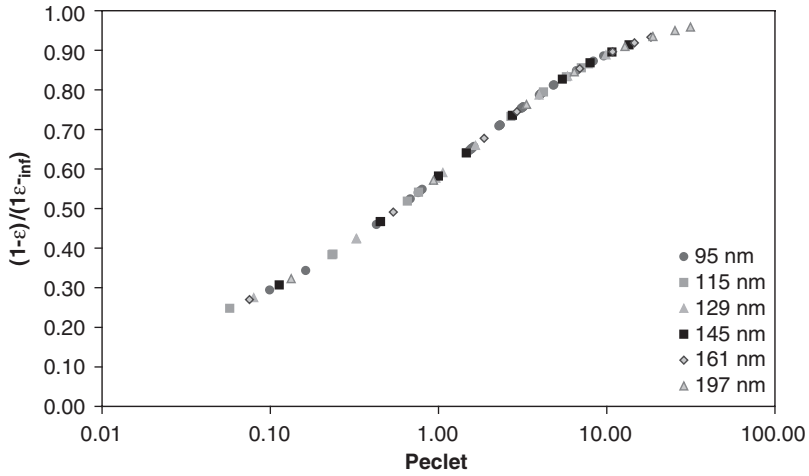

FIG. 10. Dependence of the soot cake porosity for different soot aggregate sizes at the prevailing Peclet number.

Equation (9) generalizes earlier porosity–Peclet number power-law correlations (Konstandopoulos *et al.*, 2002) obtained at $Pe > 0.3$ down to the diffusion limited deposition limit. Pe_0 is a characteristic cross-over Peclet number defining the scale beyond which the convective mechanism will take over the diffusive mechanism of deposition and ε_∞ the large Peclet number asymptote of the porosity. ε_∞ has a dependence on the aggregate size and it is described in a forthcoming publication (Konstandopoulos, 2007). Using Eq. (9) the experimental data of Fig. 9 can be collapsed on a single curve as shown in Fig. 10.

D. SOOT DEPOSIT COMPACTION

The experiments performed with the CAST burner that were reported in the previous section involved the loading of flat disk-shaped glass-fiber filters at different Peclet numbers, which was achieved by changing the sampling flow for each case. The data were analyzed using our filter pressure drop model accounting for gas compressibility, originally introduced in Skaperdas and Konstandopoulos (2001) and Konstandopoulos and Kladopoulou (2003) as shown in Fig. 11, since experimental pressure drops sometimes reached 300 mbar at the high Peclet number limit. The effect of gas compressibility forces the pressure drop signal to deviate from a linear behavior, however, the experimental pressure drop as a function of mass loading observed, remained linear throughout the experimental range of pressure drops. This is an indication that the hydrodynamic resistance factor $(\rho \times k)_{\text{soot}}$ of the deposit

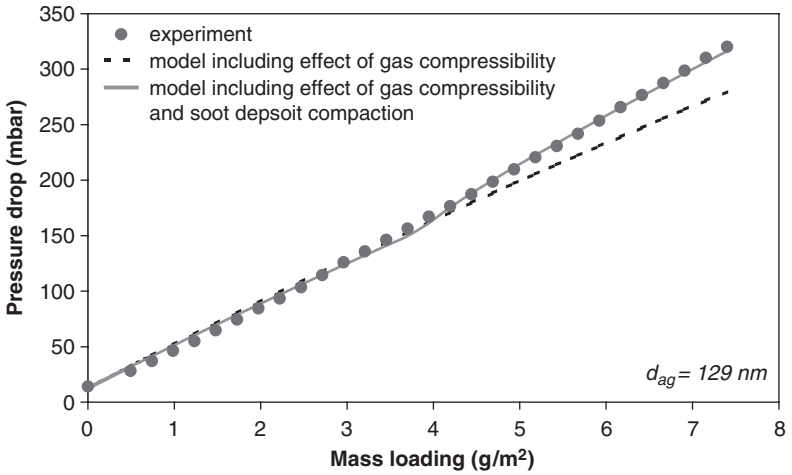

FIG. 11. Experimental filter pressure drop as a function of soot mass loading compared with the model taking into account the effect of gas compressibility (dashed line) and the effect of soot deposit compaction (continuous line). The indicative example is given for a soot aggregate size of 129 nm.

changed at higher values of the pressure drop, hence soot cake compaction was taking place. To account for deposit compaction a power law of the form was introduced:

$$\frac{\phi}{\phi_0} = \left(\frac{\Delta P - \Delta P_{\mathrm{cr}}}{\Delta P^*}\right)^{\delta} \tag{10}$$

where ϕ denotes the solid fraction and ϕ_0 the solid fraction of the deposit in the uncompacted stage. ΔP_{cr} is the critical or yield pressure drop for deposit compaction to set-in and ΔP^* a scaling constant to make the equation dimensionally correct. This simple deposit compaction model treats the deposit as a Bingham-type of material that remains undeformed below a yield pressure and that deforms with a power law in the post-yield region. The result is shown in Fig. 11 as the solid line and illustrates that at high pressure drops the effect of gas compressibility and soot cake compaction are opposing each other.

Figure 11 gives an indicative example of the effect of gas compressibility and soot deposit compaction on the filter pressure drop for a soot aggregate size of 129 nm, but the same phenomenon was observed for all aggregate sizes at sufficiently high values of the pressure drop. Based on application of the extended pressured drop model that accounts for deposit compaction, we were able to obtain for the first time a quantitative demonstration of the effect of pressure drop on soot deposit compaction. As shown in Fig. 12 critical pressure drops for soot cake compaction are setting in the vicinity of 200 mbar causing a gradual increase

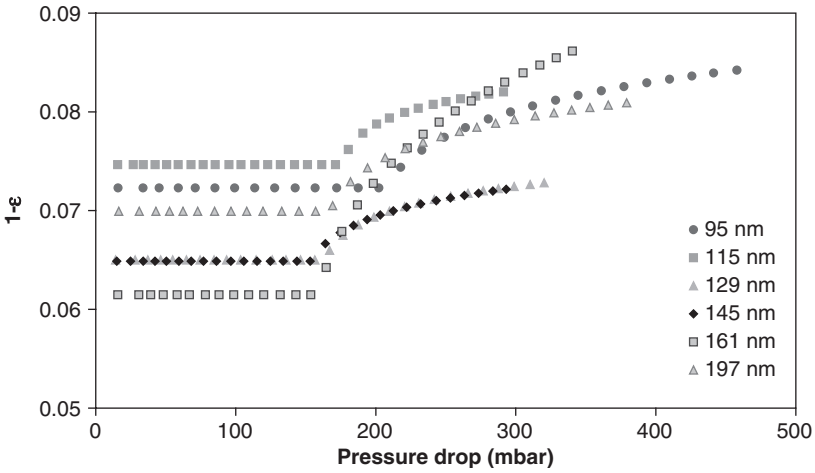

FIG. 12. Effect of pressure drop on the solid fraction of soot cake deposits as a function of soot aggregate size.

of the solid fraction ($1-\varepsilon$) of the soot deposit, which can reach 25–30% for some aggregates at high enough values of the pressure drop (>400 mbar). These pressure drops are non-typical for regular DPF operation but could instantaneously occur in a heavily loaded, undersized filter, say at the start of a forced regeneration event. Our results demonstrate that such phenomena when present can be quantitatively incorporated within the general simulation framework using the simple deposit compaction model mentioned above. ΔP_{cr} and the exponent δ in Eq. (10) have a dependence on aggregate size and morphology as is described in a forthcoming publication (Konstandopoulos, 2007).

E. Deep-bed Filtration

The introduction of more porous wall structures necessitates a closer look at the soot particle fate inside the wall and the deep-bed filtration mode starts to be important. Flow in porous media represents a challenging area of fluid mechanics and initial approaches (Bissett, 1984; Konstandopoulos *et al.*, 2001, 2003) have employed so-called unit-cell models, where the porous filter wall is approximated as a collection of "cells", each hosting an object of simple geometry (a sphere for granular filters and a cylinder for fibrous filters).

This filtration theory and a local re-computation of the evolving unit-cell geometry due to deposition of particles (Fig. 13) was employed and a transient filtration model has been derived and tested with very good success against experimental data with ceramic, metallic and fibrous filters (Bissett and Shadman, 1985; Zarvalis *et al.*, 2003). In addition, the same unit-cell-based

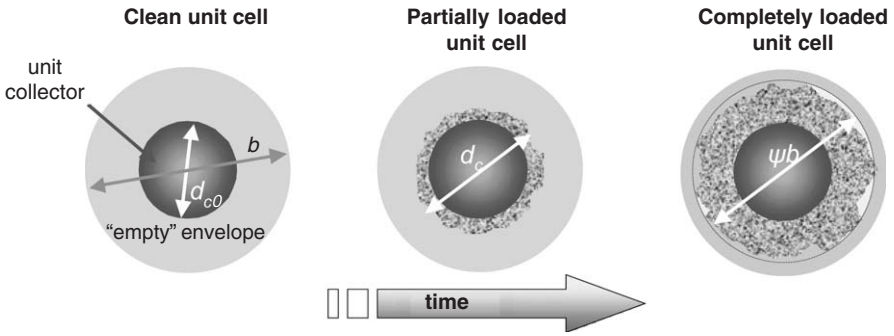

FIG. 13. Unit-cell filtration model. The collector size d_c and the empty envelope b are matched to the macroscopic porosity of the filter. The unit-cell blocks when the size of the collector becomes a fraction ψ of b (Konstandopoulos *et al.*, 2000; Vlachos *et al.*, 2002).

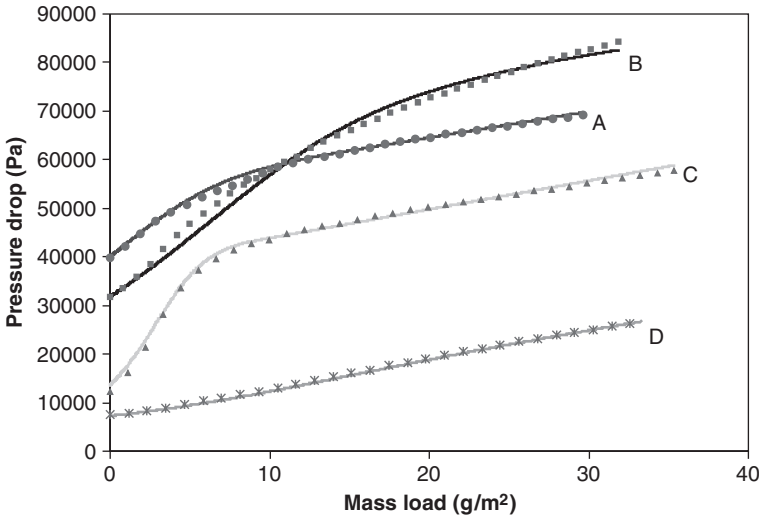

FIG. 14. Comparison of simulated pressure drop for different filters (A–D) due to catalyst deposition (solid lines) to the experimental data (points) (Karadimitra *et al.*, 2004).

filtration model has been successfully employed as a virtual sensor to describe on-line the deposition process of inorganic nanoparticles on different filter media (Karadimitra *et al.*, 2004). As seen in Fig. 14 the loading of deep-bed filters A–C is described equally successfully as the loading of the cake filter D (Karadimitra *et al.*, 2004).

The evolution of the non-uniform spatial profile of the inorganic nanoparticles deposited, across the filter wall, can be seen in Fig. 15 along with a typical SEM line scan of the distribution of an element of the

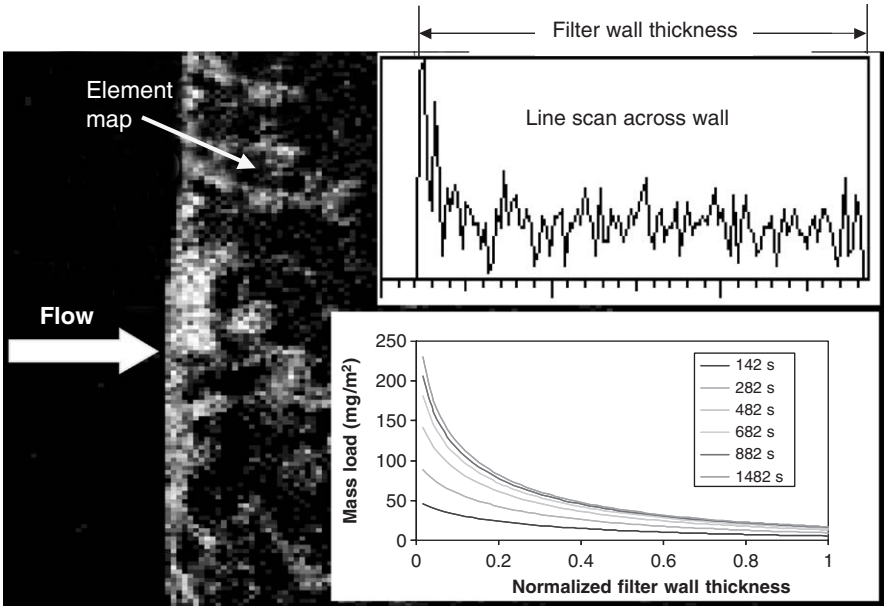

FIG. 15. Typical evolution of the spatial deposition of inorganic nanoparticles inside a porous filter wall.

nanoparticle that serves as a tracer. Both simulated and experimental profiles exhibit a sharp decay along the wall as expected from filtration theory for the particular filter structure employed.

Employing our transient filtration unit-cell model for parametric studies we can then obtain the spatial distribution and amount of nanoparticles (soot or inorganic e.g. ash or catalysts) deposited in a porous wall as a function of flow velocity and filter microstructure. This can be achieved for different types of porous materials in terms of porosity, pore size and wall thickness. Table I shows the test matrix employed for the parametric study where a wide range of filtration velocities is covered (2–10 cm/s), for a low porous ($d_{\text{pore}} = 12\,\mu\text{m}$, $\varepsilon = 40\%$) and a high porous material ($d_{\text{pore}} = 40\,\mu\text{m}$, $\varepsilon = 70\%$), and for a small and a large wall thickness ($w_s = 0.305$ and 0.432 mm corresponding to 12 and 17 mil, respectively).

The filtration model gives the mass deposited across the wall thickness at different stages of the deep-bed filtration, which are reported as the utilized capacity of the filter wall, defined as:

$$\text{Utilized capacity} = \frac{V_{\text{solid}}}{V_{\text{void}}} \tag{11}$$

where V_{solid} is the total volume of the mass collected inside the filter wall at each stage and V_{void} is the empty space inside the porous wall.

TABLE I
TEST MATRIX FOR PARAMETRIC STUDY WITH TRANSIENT FILTRATION UNIT-CELL MODEL

Filtration velocity (cm/s)	Pore size d_{pore} (μm)	Porosity ε (%)	Wall thickness w_s (mm)
2	12	40	0.305
			0.432
	40	70	0.305
			0.432
4	12	40	0.305
			0.432
	40	70	0.305
			0.432
10	12	40	0.305
			0.432
	40	70	0.305
			0.432

Figure 16 shows the normalized mass distribution inside the filter wall vs. the normalized wall thickness as a function of the utilized capacity of the filter wall, for the low porous and the high porous material (small wall thickness) at a filtration velocity of 4 cm/s. The line of the highest utilized capacity gives the state of loading inside the filter wall when the transition from the deep-bed to cake filtration has occurred and there is no more mass entering inside the filter wall. This final state of the mass distribution along the filter wall thickness was calculated for all the cases listed in Table I and the results are shown in Fig. 17.

Figure 17 shows that a more uniform mass distribution can be achieved at higher filtration velocities, both for the low and the high porous material. Finally, Fig. 18 shows the utilized capacity of the filter wall for all the cases in study, computed with a gas temperature of 280°C and a primary and aggregate particle size of 20 and 90 nm, respectively, as a function of the Peclet number. It is seen (Fig. 18) that the more porous materials with a smaller wall thickness can attain a better usage of the capacity of the filter wall, when the Peclet number increases.

F. MICROFLOW DEPOSITION IN FILTER WALL

The reconstructed "digital materials" previously mentioned are another way to simulate soot deposition apart from the unit-cell models. An example of soot deposition in such a "digital material" (reconstructed with a process-based algorithm that creates and sinters grains from a pre-computed "grain library") is shown in Fig. 19(a). As time passes the transition from deep bed to cake filtration as the top regions of the filter gets filled with soot is evident in

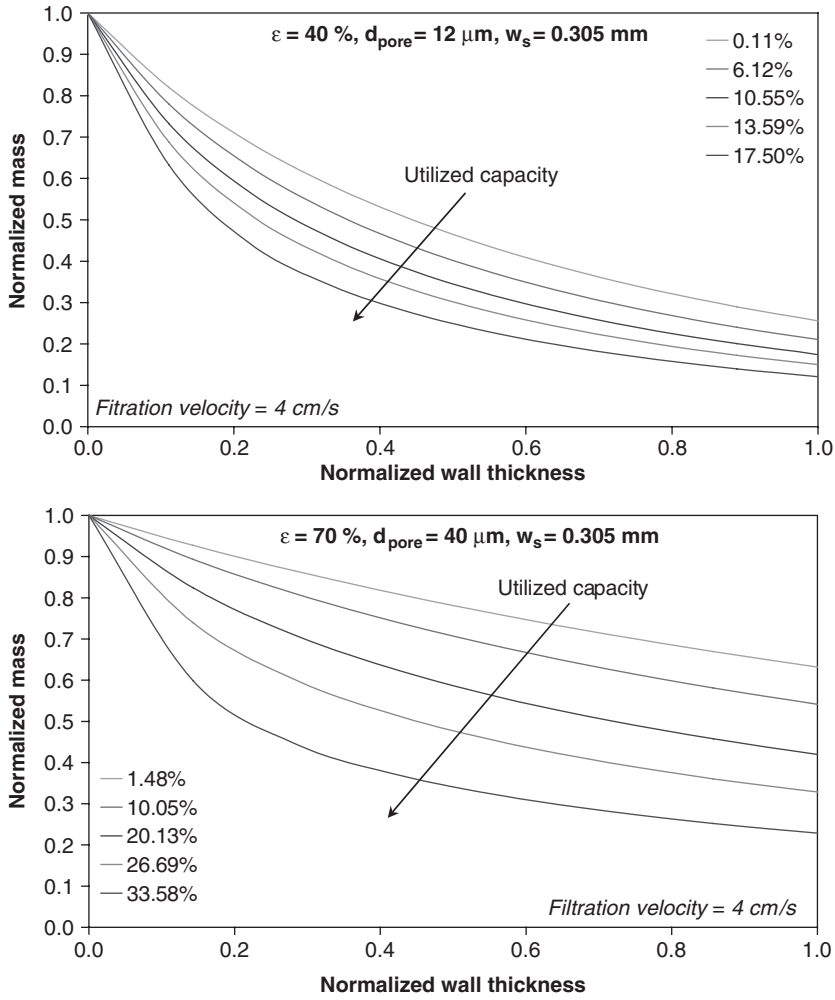

FIG. 16. Normalized mass distribution inside the filter wall vs. the normalized wall thickness as a function of the utilized capacity of the filter wall. Low porous material (top) and high porous material (bottom), for a filtration velocity of 4 cm/s and a wall thickness of 0.305 mm.

Fig. 19(b). The jumps in the curve are due to the filling of distinct "pores" which is studied in detail using this technique.

Over a macroscopic filter area these "incoherent" jumps would average out each other leading to a smooth evolution of the pressure drop as that in Fig. 14. The type of simulation shown in Fig. 19 is expected to be largely applicable in the near future for industrial use exploiting grid-computing environments (http://www.unizar.es/flowgrid/).

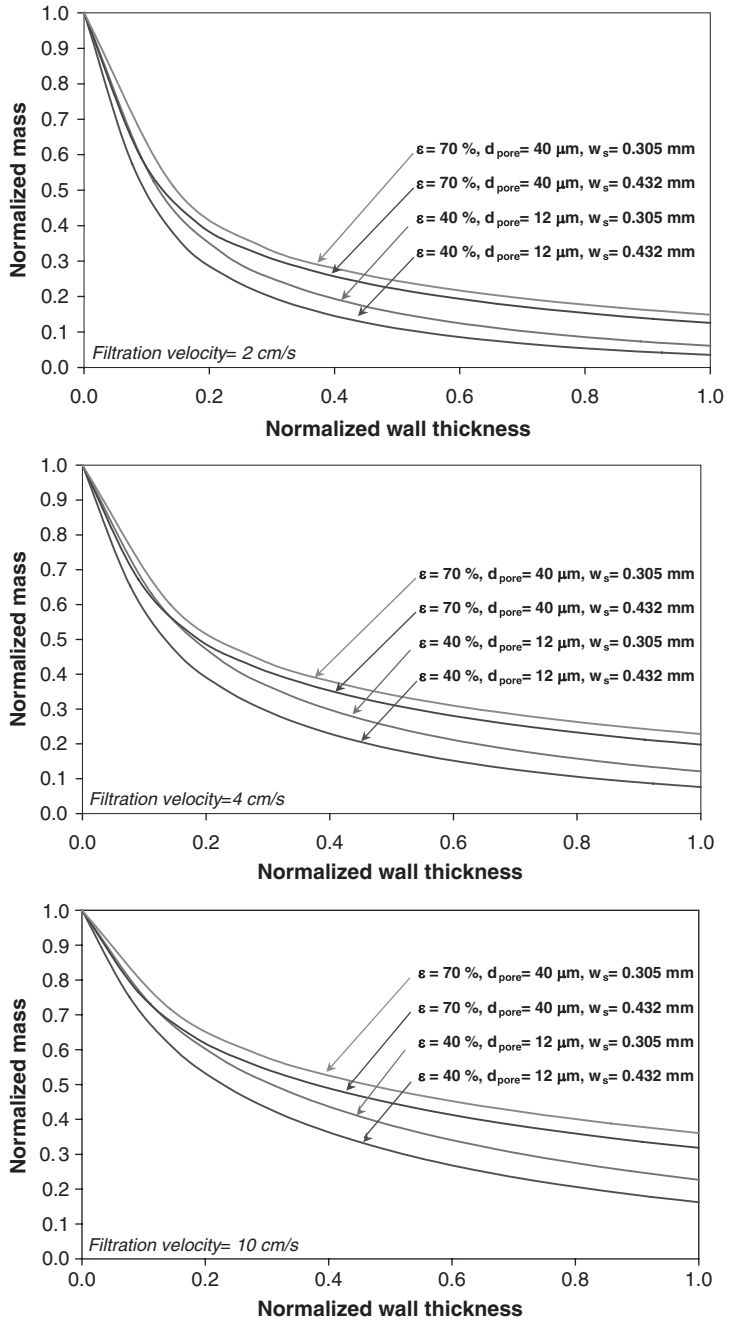

FIG. 17. Normalized mass distribution inside the filter wall vs. the normalized wall thickness for the different porous materials. From top to bottom: filtration velocity of 2, 4 and 10 cm/s.

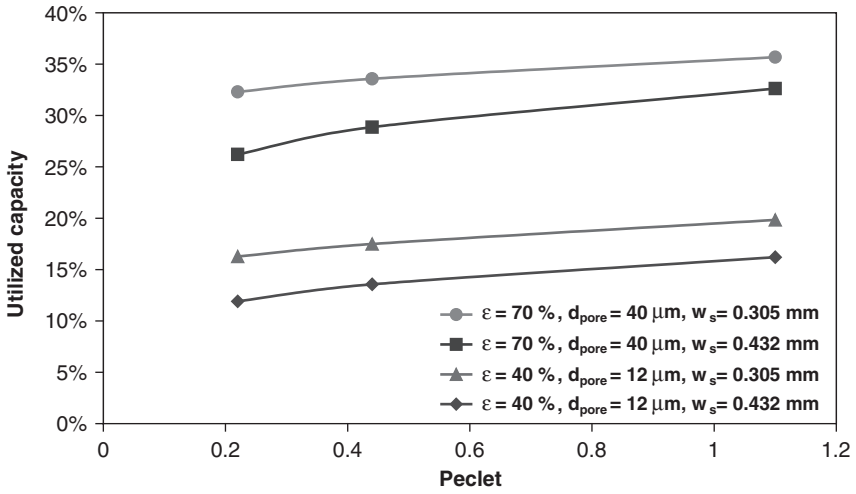

FIG. 18. Utilized capacity of the filter wall vs. the Peclet number for all the loading cases in study.

Current research efforts are concentrating on computationally efficient implementations of the energy equation within the MicroFlowS framework to allow realistic simulations of soot particle reaction in the porous structures. The next section shows a parallel line of development that started in Konstandopoulos and Kostoglou (2004), which tries to extend continuum models of soot oxidation to account for microstructural effects.

G. Effect of Microstructure on Oxidation Kinetics

The simplest phenomenological macroscopic description of a catalytic coating (Fig. 20) is represented by the so-called two-layer model introduced in Konstandopoulos and Kostoglou (1998, 1999b, 2000). The catalyst coating can interpenetrate/overlap partially with the top part of the filter wall. Hence a spatial "field of catalyst activity" can be assigned to Layer I. Above the catalyst-influenced layer a normal soot deposit exists that can only react through a thermal oxidation mechanism. The model of soot oxidation incorporating the soot layer microstructure, previously developed in Konstandopoulos and Kostoglou (2004) is combined with the two-layer model of the catalytic coating. The mathematical model is presented in detail in the appendix section.

The dimensionless microstructural parameter α accounts for the penetration of the thermal layer into the catalytic one, caused by the progressive reaction of the soot, which is in contact with the catalyst. Results are presented for different values of α (see appendix) in Fig. 21. The two layers remain separate for values of α close to 1. As α decreases the degree of penetration between the layers

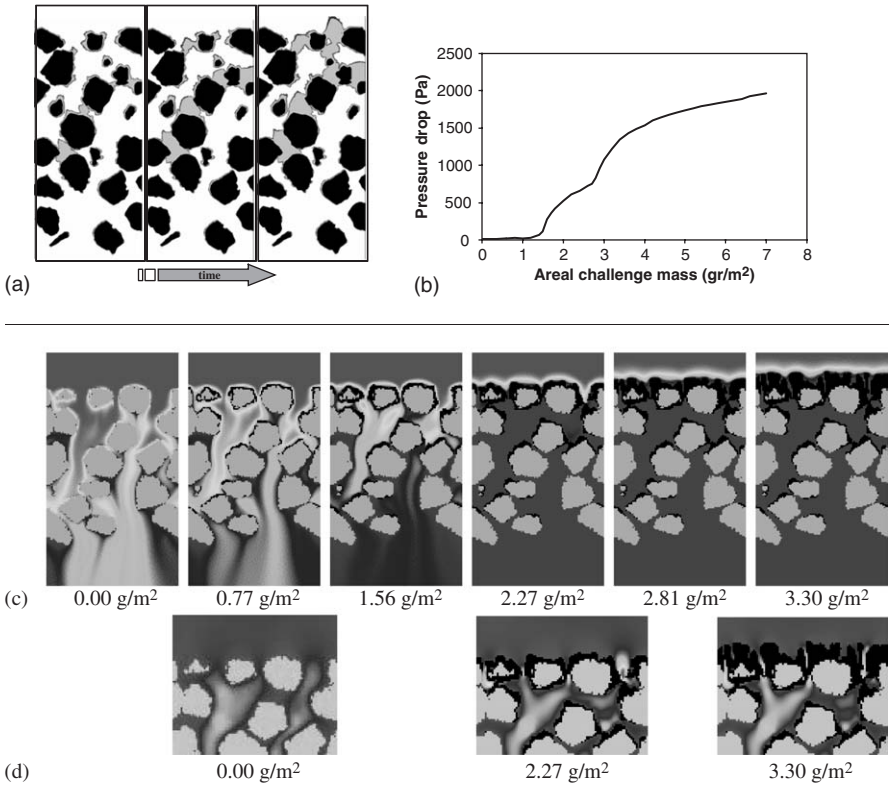

FIG. 19. Simulation of soot deposition on a filter wall. (a) Evolution of soot deposits (gray) in the wall (black is solid, white is pore space) and incipient cake formation; (b) pressure drop as function of challenge soot mass demonstrating the deep-bed to cake filtration transition; (c) visualization of soot deposition in an extruded ceramic (granular) filter wall and (d) development of soot deposits (black) and soot mass fraction in the wall (solid material is gray) to the onset of cake formation. Soot mass fraction scale is from 0 (violet) to the inflow value (red). In (d) the velocity on a section through the filter wall is shown, with overlay of the soot deposit shapes (see Plate 9 in Color Plate Section at the end of this book).

increases, leading to enhanced oxidation rates as more soot from the top layer enters the field of activity of the catalyst.

For $\alpha = 1$, soot in the catalytic layer is oxidized fast leaving the soot in the thermal layer unreacted. This has been observed with some early catalytic filters. As α decreases the soot from the top layer replaces more rapidly the soot oxidized in the catalytic layer increasing the global oxidation rate. The corresponding soot layer thickness evolution is shown in Fig. 22. For values of α close to 1 (e.g. 0.9) the catalytic layer is totally depleted from soot at some instances, followed by sudden penetration events from the soot of the thermal layer. These events are clearly shown in the thickness evolution for $\alpha = 0.9$ in

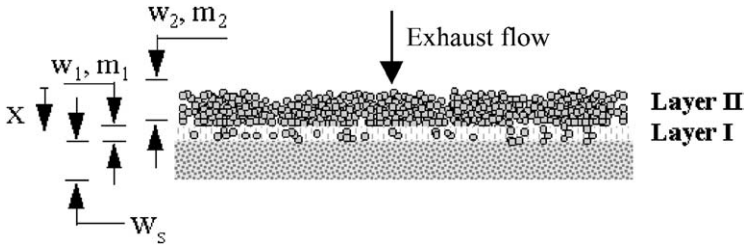

FIG. 20. Schematic of the two-layer model of catalytic coating.

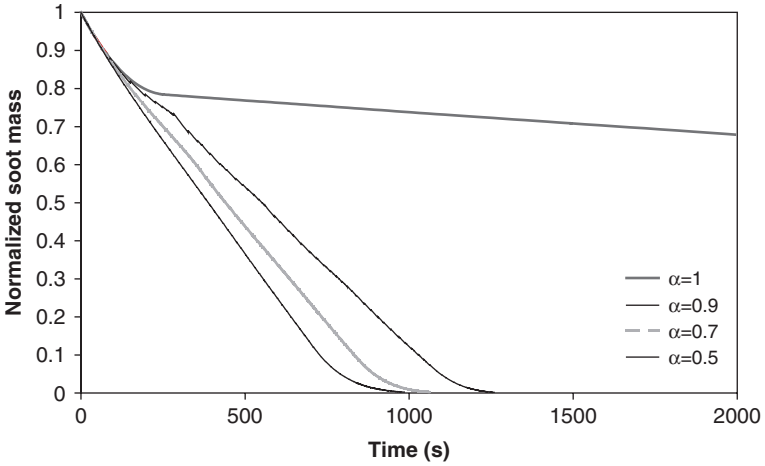

FIG. 21. Normalized soot mass evolution for different values of the microstructural parameter α.

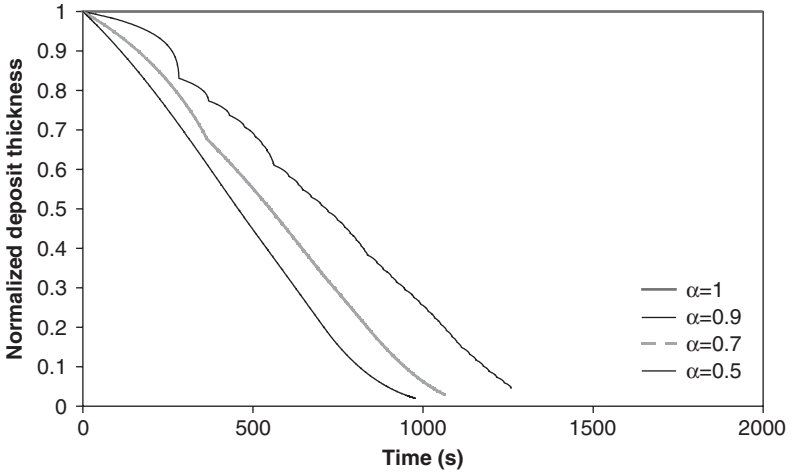

FIG. 22. Normalized soot deposit thickness evolution for different values of the microstructural parameter α.

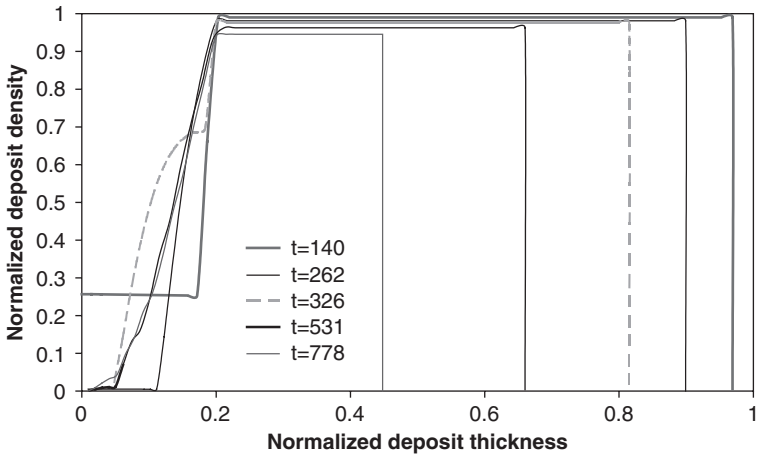

FIG. 23. Normalized soot deposit density profile for different times.

Fig. 22. For smaller values of α, equilibrium between the soot entering the catalytic layer and the soot oxidized in it is established leading to a constant global oxidation rate.

The evolution of the dimensionless density profile across the soot layer is shown in Fig. 23. The initial gradual replenishment of the soot in the catalytic layer (at $t = 140$ s) is followed by sudden penetration events ($t = 262$ and 326 s) before the establishment of a steady state profile (at $t = 531$ and 778 s). Regarding the non-catalytic (thermal) layer only a gradual reduction of its thickness, accompanied by a very small reduction of its uniform density is observed. This simple microstructural model exhibits a rich dynamic behavior, however we have also established an experimental program to study the soot cake microstructure under reactive conditions.

This is achieved by performing *in situ* permeability experiments on partially reacted soot cakes. Figure 24 shows an example of such experiments, where the evolution of the soot cake hydrodynamic resistance $(\rho \times k)_{\text{soot}}$ as a function of remaining soot mass in the filter is depicted. The experiments are performed exposing small filter samples (preloaded with soot from a modern passenger car diesel engine), in a dedicated flow reactor (Konstandopoulos *et al.*, 2000) at constant temperature. By cycling between an oxidative (10% O_2) exhaust gas and an inert (N_2) gas stream we obtain at each step controlled, partially oxidized soot cakes. These are then analyzed *in situ* with the method described in Konstandopoulos *et al.* (2002) to obtain their hydrodynamic resistance, $(\rho \times k)_{\text{soot}}$ by varying the inert gas flow rate and recording the induced pressure drop.

The method has a good resolution since it allows the distinction of $(\rho \times k)_{\text{soot}}$ for catalyzed and uncatalyzed filters. Such data in conjunction with the

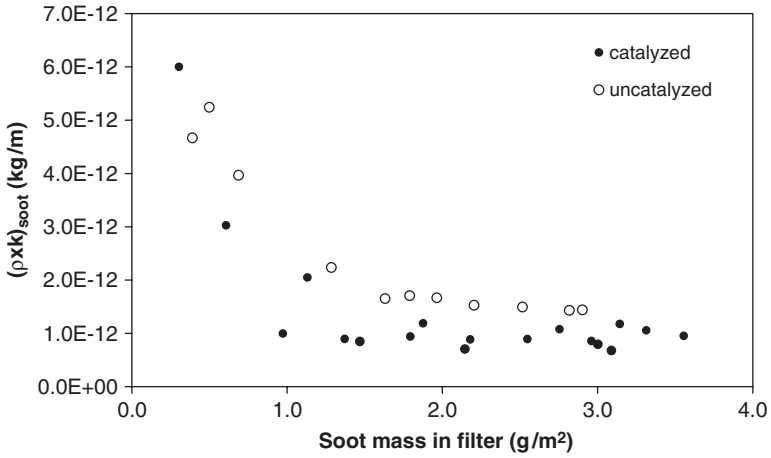

FIG. 24. Experimental determination of the change of $(\rho \times k)_{soot}$ during oxidation. At the soot mass load of 1 g/m^2 the soot cake starts to vanish and its hydrodynamic resistance starts to increase rapidly.

theoretical developments on continuum microstructural models of soot oxidation are expected to improve our description of the relevant phenomena in state-of-the-art DPF simulation tools.

H. The Role of NO_2 Turnover/Recycling

The influence of NO_2 on soot oxidation, in conjunction with a highly selective NO to NO_2 oxidation promoting catalytic coating on a DPF was studied for the first time experimentally and theoretically in Konstandopoulos *et al.* (2000). At that time NO_2-regenerative technologies were practiced with uncatalyzed filters (Hawker *et al.*, 1997; Lueders *et al.*, 1999) and it was suggested that combinations of NO_2-regenerative technologies with catalytic filters could lower the dependence of NO_2-regenerative technologies on high engine-out NO_x concentrations, as NO_x emission standards become tighter. This has now become industrial practice (Konstandopoulos *et al.*, 2004).

The following reactions occur in presence of an NO oxidation promoting catalyst (such as Pt) in the catalytic layer of the two-layer model (Konstandopoulos *et al.*, 2000):

$$C + NO_2 \rightarrow CO + NO \tag{12}$$

$$NO + \tfrac{1}{2}O_2 \leftrightarrow NO_2 \tag{13}$$

The reaction of NO_2 with soot has attracted considerable interest in the literature (Jacquot *et al.*, 2002; Olsson *et al.*, 2001) and complex reaction schemes are being developed to account for the influence of H_2O, SO_2, the collaborative effect of O_2–NO_2, presence of various catalysts on the NO to NO_2 oxidation (precious and non-precious metals), inhibition and transient kinetic phenomena, or diffusional transport limitations (Dardiotis *et al.*, 2006; Knoth *et al.*, 2005; Olsson *et al.*, 2001). While a detailed kinetics approach may lead to more elaborate rate laws, it is acceptable to consider that the soot-NO_2 and NO oxidation reaction rates are first order in NO_2. Furthermore, we consider that the catalyst and soot cake are overlaping over a spatial region of finite dimensions and no sharp boundary exists between them. As a consequence NO_2 can always find soot to react with and there are no transport limitations. This is a consequence of the realistic morphology of "rough" catalyst coatings but it also allows a great simplification in the mathematical formulation, leading to an analytic global expression for the NO_2 turnover (or recycling) factor within the framework of the two-layer model of a catalytic coating as shown in the following:

Let X and Y be the molar concentrations of NO_2 and NO and X_o and Y_o be these concentrations in the inlet stream, respectively. Then, $Z=X+Y$ is the total NO_x concentration. Let k_1 be the reaction rate constant of the soot-NO_2 oxidation reaction and k'_A and k_B the forward and backward rate constants for the NO oxidation, respectively. For the case of constant oxygen concentration across the soot layer the forward reaction can be considered of pseudo-first order with a modified rate constant $k_A=k'_A[O_2]^{0.5}$.

The two-layer model for soot oxidation with NO_2 in a catalytic filter can be written as follows:

Soot layer (thickness w_2)

In this layer only soot oxidation by NO_2 happens:

$$u_w \frac{dX}{dz} = -k_1 X \tag{14}$$

with initial condition $X(0) = X_o$

The resulting NO_2 concentration distribution is:

$$X = X_o e^{-(k_1 z/u_w)} \tag{15}$$

The NO_2 and NO concentrations leaving the soot layer and entering the catalyst layer are X_i and Y_i, respectively and they can be computed as:

$$X_i = X_o e^{-(k_1 w_2/u_w)} \text{ and } Y_i = Z_o - X_i \tag{16}$$

Soot + catalyst layer (thickness w_1)

In this layer both soot and NO oxidation take place:

$$u_{\mathrm{w}}\frac{\mathrm{d}X}{\mathrm{d}z} = -k_1 X + k_{\mathrm{A}} Y - k_{\mathrm{B}} X \tag{17}$$

$$u_{\mathrm{w}}\frac{\mathrm{d}Y}{\mathrm{d}z} = k_1 X - k_{\mathrm{A}} Y + k_{\mathrm{B}} X \tag{18}$$

with initial conditions $X(0) = X_i$ and $Y(0) = Y_i$

The resulting NO_2 concentration distribution is:

$$\mathrm{X} = \frac{k_{\mathrm{A}} Z_o}{k_1 + k_{\mathrm{A}} + k_{\mathrm{B}}} + \left(X_{\mathrm{i}} - \frac{k_{\mathrm{A}} Z_o}{k_1 + k_{\mathrm{A}} + k_{\mathrm{B}}}\right)\mathrm{e}^{-(k_1 + k_{\mathrm{A}} + k_{\mathrm{B}})\frac{z - w_2}{u_{\mathrm{w}}}} \tag{19}$$

The total reaction rate for each layer is given by integrating the local rate along the respective layer thickness (i.e.):

$$\frac{\mathrm{d}m_i}{\mathrm{d}t} = -M_{\mathrm{c}} k_1 \int_{w_{i-1}}^{w_i} X \mathrm{d}z \tag{20}$$

where w is obtained from the local value of the soot density ρ and the area mass load m_i and $w_0 = 0$ is taken as the filter surface.

The evolution equation for the two layers in the thin soot deposit limit (used here for analytical convenience) are:

$$\frac{\mathrm{d}m_1}{\mathrm{d}t} = -M_{\mathrm{c}}\frac{k_1}{k_1 + k_{\mathrm{A}} + k_{\mathrm{B}}} \left[k_{\mathrm{A}} Z_o w_1 + u_{\mathrm{w}}\left(X_i - \frac{k_{\mathrm{A}} Z_o}{k_1 + k_{\mathrm{A}} + k_{\mathrm{B}}}\right)(1 - \mathrm{e}^{-((k_1 + k_{\mathrm{A}} + k_{\mathrm{B}})w_1/u_{\mathrm{w}})})\right] \tag{21}$$

$$\frac{\mathrm{d}m_2}{\mathrm{d}t} = -M_{\mathrm{c}} u_{\mathrm{w}} X_o (1 - \mathrm{e}^{-(k_1 w_2/u_{\mathrm{w}})}) \tag{22}$$

From the above equations the evolution equation of the catalytic layer can be written in terms of that of a non-catalytic layer multiplied by a recycling factor R given as following:

$$R = \frac{C_1 C_2 C_3}{1 + C_3 + C_4} + \frac{1}{1 + C_3 + C_4}\left(1 - \frac{C_2 C_3}{1 + C_3 + C_4}\right)(1 - \mathrm{e}^{-(1 + C_3 + C_4)C_1}) \tag{23}$$

where $C_1 = k_1 w_1/u_{\mathrm{w}}$, $C_2 = Z_o/X_i$, $C_3 = k_{\mathrm{A}}/k_1$, $C_4 = k_{\mathrm{B}}/k$

The NO_2 turnover or recycling factor R then means the number of times an NO_2 molecule is re-used to oxidize soot compared to the absence of a catalytic coating promoting NO into NO_2 oxidation. The recycling factor for the case of an exhaust stream containing NO_2 entering the catalytic layer at equilibrium conditions is shown in Fig. 25 vs. the parameter C_3 (affected mainly by the design variable catalyst content which affects k_A) for several values of C_1 (affected by design and operational variables wall velocity, catalyst layer thickness). In the case of large C_3 the recycling factor R attains its maximum value and therefore it is a useful number to know for design/optimization purposes.

$$R_\infty = C_1 \frac{[NO_2]_{eq}}{[NO_2]_i} \tag{24}$$

Based on the NO_2-soot oxidation data promoted by the catalytic coating tested in Konstandopoulos *et al.* (2000) an R value of about 3.4 has been computed. This represents a significant enhancement.

The above approach of integrating analytically (under certain assumptions) across the porous wall the species balances to obtain local soot consumption rates can be extended for the case of more reactions occurring in the porous wall. In the presence of a precious metal catalyst, the hydrocarbons and the carbon monoxide of the exhaust gases are also oxidized. It can be assumed that all the reactions in the porous wall occur hierarchically (according to their

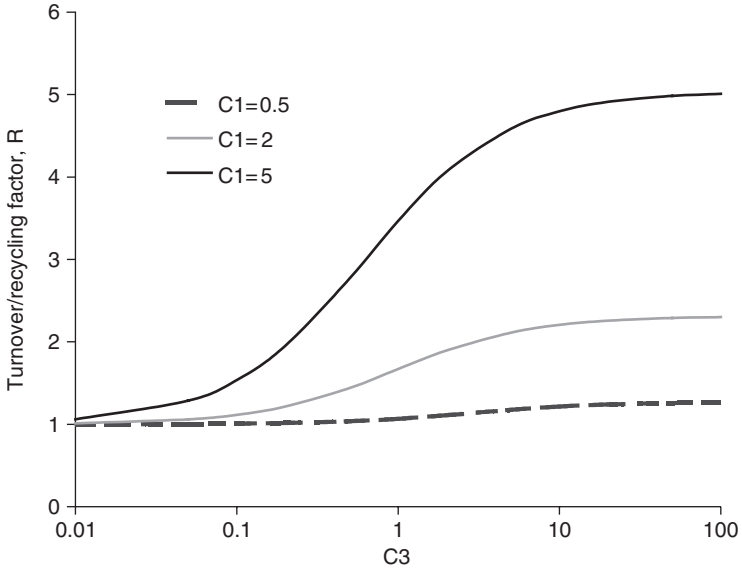

FIG. 25. Recycling factor R vs. parameter C_3 for several values of parameter C_1.

kinetics) permitting the analytical integration of the mass balances and the derivation of closed form relation for the local reaction rates (Konstandopoulos *et al.*, 2007). A further extension of this approach to include mass transfer effects which may be important in case of high reaction rates is also possible.

IV. Filter Channel Scale

The next relevant spatial scale is that of the filter channel. If the inlet conditions to the DPF can be assumed to be spatially (radially) uniform, formulating the DPF simulation model for two representative channels (inlet and outlet) is equivalent to solving it for the entire DPF (assumed radially homogeneous). It is not therefore surprising that this scale claims most of the published works in the literature, starting with Bissett (1984) who formulated the first comprehensive model which takes into account the detailed flow distribution in the channel. As the transient behavior of the monolith is slow with respect to the residence time of the exhaust gas as it travels across the filter, the quasi-steady state approximation for the exhaust flow in the channels simplifies considerably the computational burden. Although the flow in the filter channels is actually 3D, it can be accurately approximated by a (perimeter averaged) one-dimensional (1D) configuration.

This has been confirmed by Konstandopoulos *et al.* (1999, 2003) who demonstrated excellent agreement of analytical solutions of a 1D single channel flow model with exact 3D Computational Fluid Dynamics (CFD) results as well as with many experiments for square and triangular shaped channels. New developments in the filter channel scale phenomena simulation include: the study of different geometrical factors and soot loading on inertial inlet/outlet channel losses, the implications of asymmetric channel geometries (for ash tolerance), the modeling of particle entrainment phenomena (for ash and soot) and the refinement of the channel-to-porous wall heat transfer modeling. These are discussed in more detail in the next sections.

A. Inertial Losses at Channel Inlet/Outlet

The contraction of the exhaust gas at the entrance of the inlet channels and its expansion at the exit of the outlet channels causes inertial losses. It has been shown in Konstandopoulos *et al.* (2001) that CFD calculations or experiments are the only means to evaluate these losses, since estimations on literature correlations (which are not specifically developed for the honeycomb structure of the DPF) are not sufficiently accurate for such evaluations. Moreover, the influence of the soot cake on these losses has never before been studied in a thorough fashion. To improve the inclusion of such phenomena in DPF

simulation tools, the effect of different cell densities and soot loadings on the DPF contraction/expansion losses coefficient ζ (Konstandopoulos *et al.*, 2001) is summarized in the present section.

3D CFD calculations were performed with a commercial CFD package (Fluent Inc., 2001) taking advantage of the symmetry of the problem. The physical domain modeled is the one shown in Fig. 26, which includes part of the inlet, the outlet channel and the wall. The computational domain also includes sufficiently large sections upstream and downstream of the channel to obtain well-developed flow. This approach for modeling DPFs has been used and validated in the past (Konstandopoulos *et al.*, 2001, 2003) where the reader can find more detailed descriptions of the procedure followed for the domain and mesh creation.

To investigate how the blocking of the channel affects the contraction/expansion losses coefficient ζ various cases were studied in terms of filter cell density, channel size and soot mass loading inside the filter. These parameters are shown in Table II, along with the frontal open area fraction (OAF or ε_A defined as the open channel area over the total filter face area) corresponding to each case. The channel length was fixed to 150 mm (which corresponds to a typical 6 in DPF), and the channel plug length was initially set to 5 mm.

The calculations were performed for a Reynolds number based on the channel hydraulic diameter (Re_h) of 1,800. This high Reynolds number was chosen since a more accurate determination of ζ can be obtained at these flow conditions (either experimental or computational) keeping in mind that inertial effects are more pronounced at high Re_h. The permeabilities of the filter wall

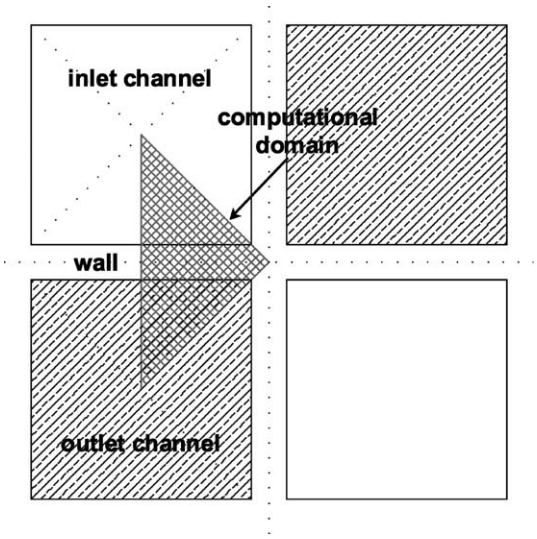

FIG. 26. Cross section of filter channels showing the front view of the CFD computational domain.

TABLE II
TEST MATRIX FOR CFD CALCULATIONS

Cell density (cpsi)	Wall thickness (mm)	Channel size (mm)	Soot layer thickness (μm)	Open area fraction
100	0.3356	2.184	0	0.370
			100	0.305
			200	0.247
200		1.440	0	0.322
			100	0.238
			200	0.168
300		1.111	0	0.287
			100	0.193
			200	0.117

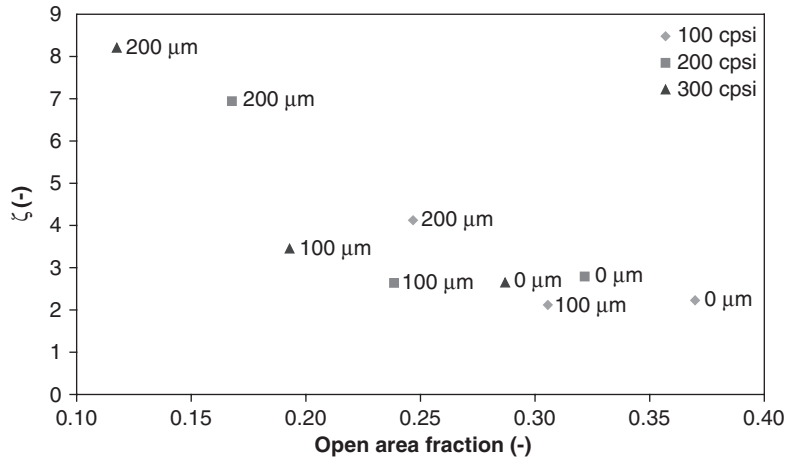

FIG. 27. Contraction/expansion losses coefficient ζ vs. open area fraction for different cell densities and soot mass loadings.

and that of the soot layer were fixed to the representative values of 1×10^{-12} and $3.3 \times 10^{-13}\,\mathrm{m}^2$, respectively. The inertial loss coefficient ζ was determined by a single CFD calculation of the pressure distribution along the system, for each case, and by subtraction of the pressure loss due to the porous channel region, and the porous soot layer (when present). The results are shown in Fig. 27 as a function of the open area fraction for the different filter cell densities and soot mass loadings.

The data clearly can be only approximately correlated in terms of the open area fraction as shown in Fig. 27. Subsequently we studied the effect of the plug length on the inertial losses coefficient ζ for a clean filter at the three different

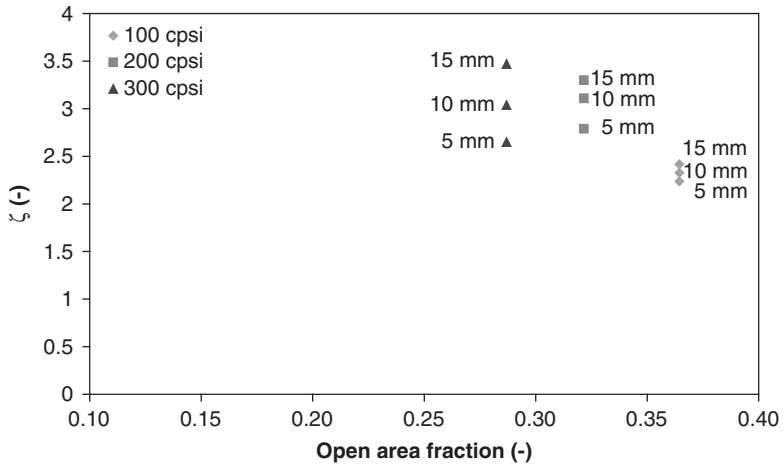

FIG. 28. Contraction/expansion losses coefficient ζ vs. open area fraction for different cell densities and plug lengths.

cell densities listed in Table II. The plug length value ranged from 5 to 15 mm and the results are shown in Fig. 28.

As it is seen the task of deriving a theoretical description for ζ requires a substantial amount of computations, but it is not intractable. Pending the derivation of a generalized correlation (that takes into account the combined effect of open area fraction, cell density, soot thickness and plug length) we employ in our simulations tabular interpolations between the data of Figs. 27 and 28, which cover a sufficiently large parameter space for practical applications. The advent of other than square channel shapes (Konstandopoulos *et al.*, 2003) or asymmetric channel designs for ash tolerance (Bardon *et al.*, 2004; Ogyu *et al.*, 2004; Young *et al.*, 2004) poses no problem as it can be handled within the same computational framework. Our current efforts with asymmetric channel geometries (see next section), however, focus on the more important problem of extending our single and multichannel DPF simulation models to account for such effects.

B. Asymmetric Channel Geometries

The Peclet number dependence of the soot cake microstructure has important implications for the morphology of the soot (and ash) deposits in the square channels of DPFs, as illustrated in Fig. 29, obtained by a mixed Ordinary Differential Equations (ODE)–Monte Carlo simulation (Rodriguez-Perez *et al.*, 2004).

Since the introduction of asymmetric designs (Bardon *et al.*, 2004; Ogyu *et al.*, 2004; Young *et al.*, 2004) the inclusion of such shape effects on DPF

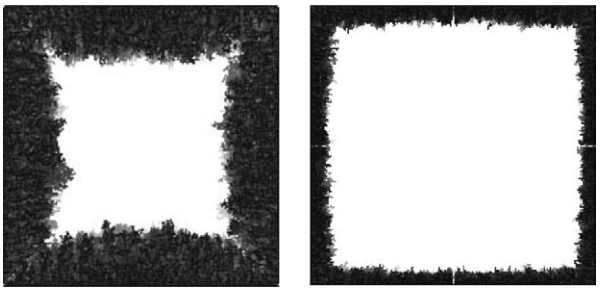

FIG. 29. Morphology of simulated soot deposit grown in a square channel for $Pe = 0.1$ (left) and $Pe = 100$ (right), at the same soot mass load in the filter (Rodriguez-Perez *et al.*, 2004).

simulation tools employed by the industry becomes necessary. As this inevitably will entail approximations these will have to be assessed with more detailed studies. Soot deposit growth and microstructure evolution is not presently accounted for in general purpose flow solvers. The "hooks" provided in all general purpose flow solvers through user defined functions/subroutines (although often quite awkward) can be used to interface in the solver phenomena occurring at the sub-grid scale and hence study the aforementioned channel shape effects. Our interfacing of local soot deposit growth to large scale CFD simulations is presented in Konstandopoulos *et al.*, 2005. In the present section, we provide examples of the current state of our developments with asymmetric filter channel shapes.

Figure 30 lists schematics of three asymmetric channel geometries (A, B and C) inspired by the designs presented in Ogyu *et al.* (2004), Young *et al.* (2004) and Bardon *et al.* (2004) studied (at the same value of open area fraction).

Figures 31 and 32 demonstrate the growth of soot cakes in each structure shown in Fig. 30. While a detailed account of soot deposit growth dynamics in asymmetric channel designs will be given elsewhere we can remark that the soot deposits grown bear a very good similarity to those shown on SEM pictures of some of the designs (Ogyu *et al.*, 2004). All filter designs after an initial stage exhibit a nearly uniform soot deposit. This demonstrates the utilization of the entire internal surface area of the inlet channels, as the flow readjusts to transport the soot particles along the path of least resistance (which is not necessarily the shortest geometric path between the inlet and outlet channel, i.e. the wall thickness). This self-regulated behavior is currently advantageously exploited to bring such asymmetric designs within the multichannel simulation framework.

C. Ash and Soot Entrainment Phenomena

The mechanistic modeling of ash transport and deposition dynamics was originally introduced in Konstandopoulos *et al.* (2003). The same formalism can

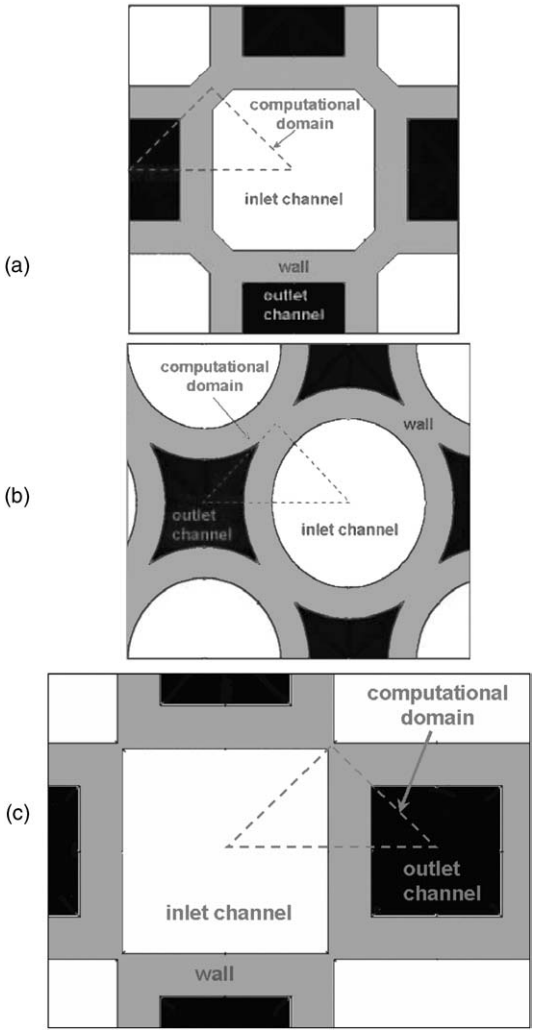

FIG. 30. Cross section of asymmetrical designs showing the front view of the CFD computational domain.

be applied to account for shear-induced soot particle re-entrainment and further downstream deposition (Peters, 2004). Experimental studies of ash deposition and transport in filters require extensive and costly engine runs and are scarce in the literature. A dynamic ash transport-deposition model is then an attractive alternative for the assessment of DPF systems with respect to ash accumulation.

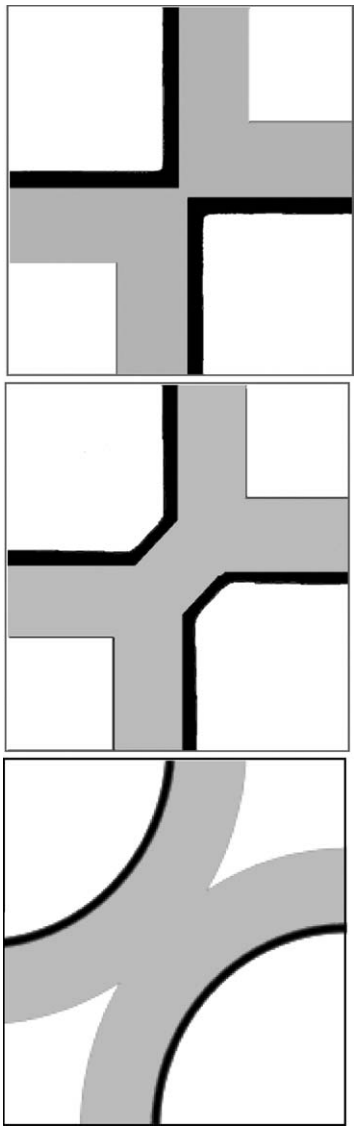

FIG. 31. Soot deposits grown on the different channel geometries a, b and c of Fig. 30.

The ash simulation model (Konstandopoulos *et al.*, 2003; Rodriguez-Perez *et al.*, 2004) consists of ash transport and ash layer evolution equations describing the interaction between ash deposition and re-entrainment in the channels along with the gas mass balance and momentum balance equations in the inlet and outlet channels of the DPF. Ash re-entrainment is initiated by flow

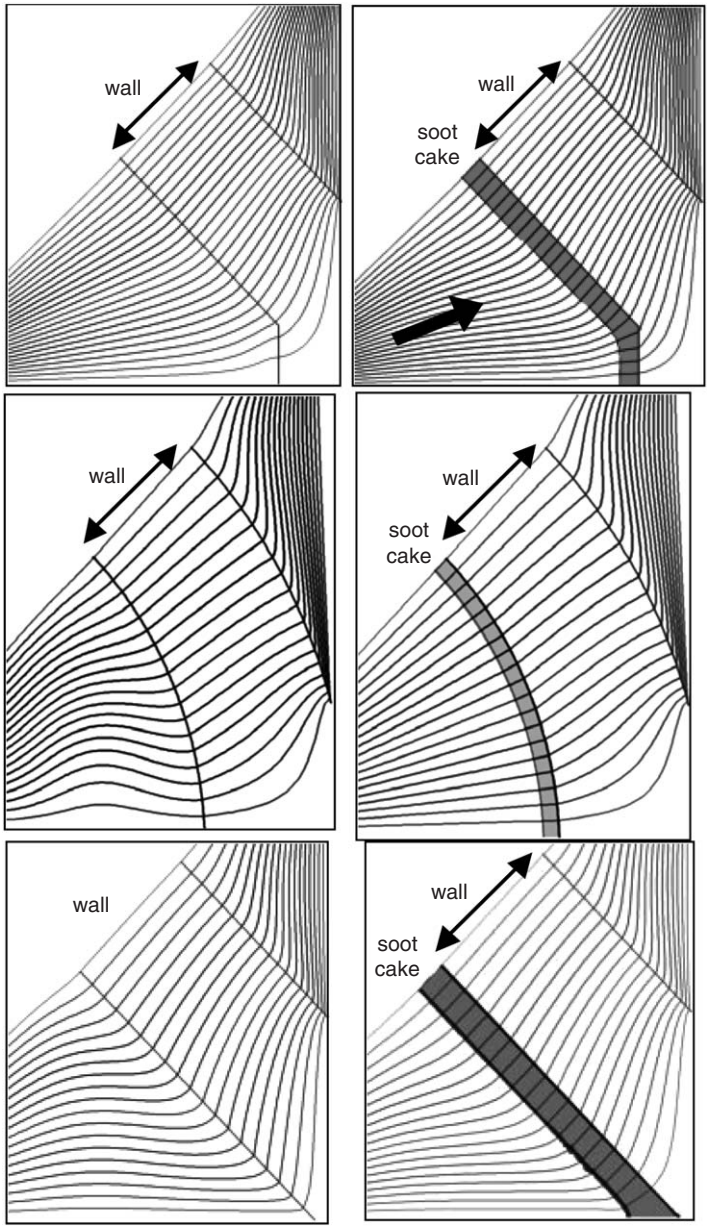

FIG. 32. Path lines (spaced at intervals of equal flux) of the wall flow in different asymmetric shape cells in clean (left) and loaded (right) states. From the top, geometries a, b and c of Fig. 30 are shown.

shear stresses along the channel, whenever the shear stress in the channel exceeds locally a critical shear stress characteristic of the ash type (as e.g. determined by composition, particle size, etc). The kinetics of ash re-entrainment are determined by the ash stickiness that for a given type of ash depends on the previous filter temperature history (currently accounted by the maximum temperature that the filter wall has experienced), as obtained by a separate filter regeneration simulation (Konstandopoulos *et al*., 2003). Ash stickiness is described by a critical ash sticking temperature by analogy to the ash fusion temperature employed in studies of ash fouling in heat transfer equipment.

The dynamic ash transport and deposition model can exhibit a rich behavior, depending on the ash quality, and prevailing flow conditions leading to different ash deposition profiles inside DPFs, despite its apparent simplicity. Sticky ash leads to deposition along the walls while non-sticky ash can be transported towards the end of the filter. A comparison to the experimental data of Bardasz *et al*. (2003) in Fig. 33 shows good quantitative agreement for the ash layer thickness resulting from different oil consumption protocols. The sulfur content of the oil and whether it is doped into the fuel (to accelerate the ash ageing test) determines its ''stickiness'', and this in turn is described by the model of ash re-entrainment. Optimized filter cell densities accounting for different ash accumulation modes and soot loading of filters have been presented in Konstandopoulos and Kladopoulou (2004).

The same approach is employed to describe shear-induced transport of soot particles. Based on limited amount of experimental information for such phenomena in the literature we have established a flow cell where soot entrainment from the surface of preloaded filters from the engine exhaust can be studied. Preliminary experiments at ambient conditions reveal that no soot entrainment is observed up to relevant shear rates at the entrance of DPFs. We attribute this to the moisture content in ambient conditions of the soot deposits that due to capillary condensation increases adhesive forces between the particles. In the future experiments at high temperatures are planned to evaluate experimentally the shear-entrained fluxes for soot and ash deposits.

D. Channel to Porous Wall Heat Transfer

A basic element of the thermal dynamics of the DPF is the heat transfer between the gas in the channel and the porous wall. In case of a porous wall having small wall thermal Peclet number Pe_T (as is always the case for a DPF as shown by Bissett and Shadman (1985)) the problem degenerates to the following modified Graetz problem:

$$\vec{u}\vec{\nabla}T = \alpha_{th}\nabla^2 T \tag{25}$$

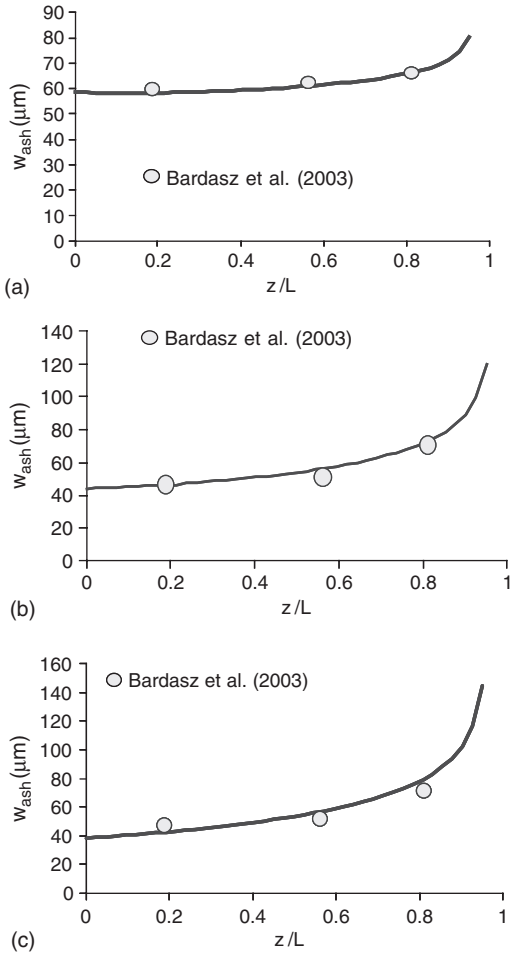

FIG. 33. Simulated ash profile along the filter length vs. experimental data of Bardasz *et al.* (2003). (a) High sulfur oil doped into fuel, (b) low sulfur oil doped into fuel and (c) high sulfur oil, regular use undoped into fuel.

with BC's $T=T_i$ at channel inlet and $T=T_w$ at porous wall, where the velocity field is obtained from the solution of the Navier–Stokes equations with the boundary condition of a constant suction velocity u_w. Our goal in developing DPF simulation tools is not the direct solution of Eq. (25) but its replacement with a 1D equation for the cross-section average (mixing-cup) temperature along the channel. This problem has been solved for the cases of a slit (two-dimensional (2D) planar geometry) and a circular pipe. Here we draw some general conclusions for arbitrary channel cross sections based on the behavior of existing solutions. For the purpose of presentation let us assume a

planar geometry with a slit width of $2L$. This geometry would be relevant for example to the DPF design studied in Konstandopoulos *et al.* (2005).

A first necessary condition for the existence of the 1D analog of Eq. (25) is the existence of a self-similar (asymptotic) velocity profile (itself equivalent to the existence of a 1D equation for the flow field). This self-similar profile depends only on the wall Reynolds (Re_w) number and has the following form (planar slit geometry):

$$u_z = \left(\overline{u}_{zo} - \frac{z u_w}{L}\right) f(y^2; Re_w) \tag{26}$$

$$u_y = \frac{u_w}{L} \int_0^y f(y^2; Re_w) \mathrm{d}y \tag{27}$$

The above self-similar velocity profiles exists only for a Re number smaller than a critical value (e.g. 4.6 for a circular pipe). The self-similar velocity profiles must be found from the solution of the Navier–Stokes equations. Then they have to be substituted in Eq. (25) which must be solved to compute the local Nusselt number $Nu(z)$. The asymptotic Nusselt number Nu_{as} for a pipe flow and constant temperature boundary condition is given by Kinney (1968) as a function of Re_w and Prandtl (Pr) numbers. The complete $Nu(z)$ curve for the pipe and slit geometries and constant temperature or constant flux boundary conditions were given by Raithby (1971). This author gave Nu_{as} as a function of Re_w and fluid thermal Peclet (Pe_T) number. Both authors solved Eq. (25) via an eigenfunction expansion.

The heat balance for the slit geometry in terms of gas mixing-cup temperature T_c is

$$2L\rho_g c_p \frac{\mathrm{d}\overline{u}_z T_c}{\mathrm{d}z} = -2h(T_c - T_w) - 2\rho_g c_p u_w T_w \tag{28}$$

From the Figs. 7 and 8 of Raithby (1971) one can infer that

$$Nu = A(Re_w) + Pe_T B(Re_w, Pe) \tag{29}$$

Substituting in the heat balance leads to

$$L\overline{u}_z \frac{\mathrm{d}T_c}{\mathrm{d}z} = -\frac{\alpha_{th}}{2L} A(Re_w)(T_c - T_w) + (1 - B(Re_w, Pe)) u_w (T_c - T_w) \tag{30}$$

The function A stands for the modification to the usual Nusselt number for non-porous wall (the so-called Graetz problem) due to the suction-distorted

axial velocity profile. Its value in the limit $Re_w \to 0$ is the well-known asymptotic Nusselt number (3.6568 for pipe). The function B stands for the heat quantity transferred by the fluid stream entering the wall. The temperature of the stream leaving the wall is actually a proper average over the cross section. This averaging process has to do with the flow field (i.e. from where this fluid is coming from) and the temperature field which is imposed by the conduction process and it must be crossed by the transversely flowing fluid. From the Raithby (1971) it seems that the function B takes values around 0.5 for small values of Re_w and Pe_T and increases as Pe_T increases for a given Re_w. The large Pe_T asymptote for B is

$$B(Re_w, Pe_T) = 1 - A(Re_w)/Pe_T \tag{31}$$

The asymptotic form of B given above is valid in every geometry since it results from the requirement for the correct heat flux direction.

The success of the 1D fluid dynamic model to describe the flow field in the DPF channel (Konstandopoulos and Johnson, 1989; Konstandopoulos *et al.*, 1999, 2003) is an indication for the existence of a (nearly) self-similar flow field. A necessary condition for the application of the 1D model for the heat transfer problem as well, is that the wall velocity u_w variation must be small along the characteristic channel length required for establishment of a steady heat transfer pattern (i.e. a length of $a^2\bar{u}_z/\alpha_{th}$). In transferring the above to the case of flow and heat transfer in a DPF channel we may formally write the heat balance as

$$a^2\overline{u}_z \frac{dT_c}{dz} = -4\alpha_{th}A(Re_w)(T_c - T_w) + (1 - B(Re_w, Pe_T))4au_w(T_c - T_w) \tag{32}$$

It must be noticed that the relative contribution of the conductive to convective heat transfer is given by the ratio

$$(1 - B)Pe_T/A(0) \tag{33}$$

which can take appreciable values (close to 1) in some practical conditions, so an accurate computation of the functions A and B is desirable and is currently in progress.

The functions A and B need to be computed for the particular geometry of the DPF channels by solving the complete flow and temperature fields for different values of the wall Reynolds, Re_w, and thermal Peclet, Pe_T, numbers and fitting the 1D Eq. (32) to the resulting average perimeter-averaged temperature evolution along the channel. Alternatively, the technique of Raithby (1971) and Kinney (1968) involving the solution for the self-similar flow field and eigenvalue analysis of the resulting energy equation (of the convection diffusion type) can be followed. For large Pe_T an asymptotic form

for B valid in any geometry is given by

$$B(Re_w, Pe_T) = 1 - A(Re_w)/Pe_T \tag{34}$$

Assuming that $Nu = A(0)$ (i.e. $B = 0$, suction does not influence the temperature profile, Bissett, 1984) can lead to an inconsistency for $Pe > A(0)$ since the heat flux is reversed from the hot wall to cold gas in the channel. In Kostoglou *et al.* (2003) the assumption of $Nu = A(0)+Pe$ (i.e. $B = 1$) was employed. This is equivalent to assuming that the gas entering the porous wall has a temperature equal to the local mixing-cup temperature of the gas flowing in the channel. This assumption ensures the correct direction of heat flux but overestimates it a bit, since the actual value of B is between 0 and 1. A very good assumption consistent with the 1D flow model is then to use $A = A(0)$ i.e. a Nusselt number applicable to a solid wall but put $B = 0.5$ as an estimation based on Figs. 7 and 8 of Raithby, 1971. This approximation leads to the following relation for the case of Prandtl number equal to 0.7:

$$Nu = 2.72 + 0.35Re_w \tag{35}$$

The above relation is very similar to the first-order expansion with respect to Re_w of the polynomial fitting of numerically obtained data for heat transfer in a square channel with one porous and three solid walls (Hwang *et al.*, 1990).

V. Entire Filter Scale

A. The Effective Conductivity of DPFs

The axial effective conductivity $\lambda_{a,eff}$ of the DPF is well known to be the product of the solid fraction $(1-\varepsilon_A)$ and the conductivity of the wall material λ_w. The open area fraction ε_A (equivalent to the porosity) of a square honeycomb structure is

$$\varepsilon_A = \left(1 - \frac{w_s}{a + w_s}\right)^2 \tag{36}$$

This wall material conductivity λ_w is also an effective conductivity since the wall is porous and it is determined from the wall porosity and intrinsic material thermal conductivity, usually through a power law relation known as Archie's Law.

The transverse effective conductivity $\lambda_{t,eff}$ requires a more involved computation. In this direction the DPF is a periodic medium, so its effective conductivity can be found by solving the heat conduction equation in the primary geometric unit (Fig. 34).

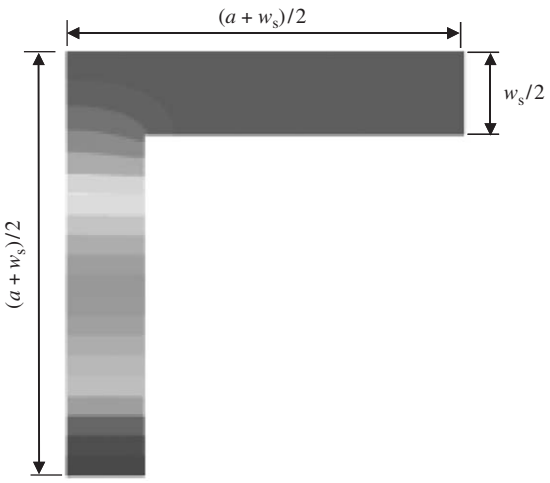

FIG. 34. Primary geometric unit for the effective conductivity of DPF (see Plate 10 in Color Plate Section at the end of this book).

A unit temperature difference is imposed to the top wall of Fig. 34 and the conductance is computed. The boundary conditions are $T=1$ at the upper side, $T=0$ at the bottom side and insulation for all the other sides. The gas conductivity is considered through the gas phase heat balance equation so is not taken into account here. Taking into account the gas conductivity to compute the transverse effective conductivity for the DPF structure is not correct.

Groppi and Tronconi approximate the conductivity of monoliths with square channels using a network of resistances analog as Gropi and Tronconi (1996):

$$\frac{\lambda_{t,eff}}{\lambda_w} = \frac{1-\sqrt{\varepsilon_A}}{1+\varepsilon_A-\sqrt{\varepsilon_A}} \tag{37}$$

A close inspection of the derivation in Gropi and Tronconi (1996) reveals that it does not retain the square network symmetry. A larger element length was assigned to the lower resistance path than the one of the higher resistance path leading to a 13% underestimation of the total resistance. Correcting the network analog assigning equal lengths to the two heat transfers paths (i.e. parallel and perpendicular to the temperature gradient in Fig. 34) leads to:

$$\frac{\lambda_{t,eff}}{\lambda_w} = \frac{a+w_s}{a+w_s/2}\left(1+\left(\frac{a+w_s}{a+w_s/2}\right)^2\right)^{-1} = \frac{2}{1+\sqrt{\varepsilon_A}}\left(1+\left(\frac{2}{1+\sqrt{\varepsilon_A}}\right)^2\right)^{-1} \tag{38}$$

The derivation of the above expression is straightforward following the technique described in Gropi and Tronconi (1996). The value of $\lambda_{t,eff}/\lambda_w$ for a typical filter with $w_s/(a+w_s)=0.2$ is: $\lambda_{t,eff}/\lambda_w=0.212$ (based on Fluent finite volume calculations), $\lambda_{t,eff}/\lambda_w=0.238$ (network approximation of Hwang *et al.*, 1990), $\lambda_{t,eff}/\lambda_w=0.211$ (improved network approximation). Commercial filters are of similar (or smaller) wall to channel ratios so Eq. (38) can be safely used for design purposes.

The validity of the effective homogeneous medium approximation to describe heat transfer in the multichannel scale will be assessed following the derivation of the Eq. (38) for the computation of the effective conductivity. For this purpose a DPF segment of square shape containing 24×24 channels is considered.

A unit temperature difference between the upper and the other three sides is assumed to achieve macroscale 2D temperature distribution in addition to the microscale one. The problem is solved using Fluent, with the results shown in Fig. 35. Heat fluxes through the right (equal to the left due to symmetry) and bottom sides are shown in Fig. 36. The fluxes from Fluent are averages along

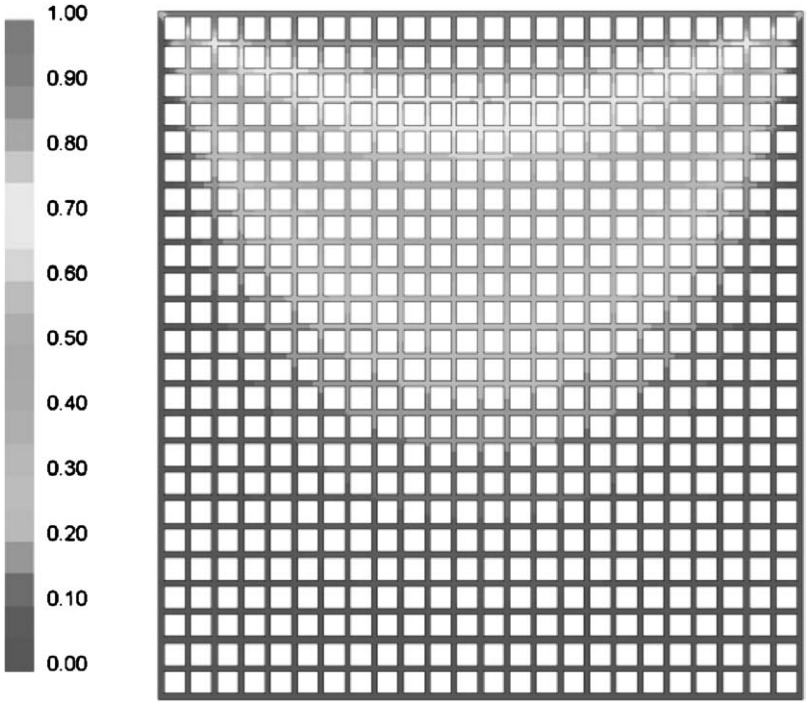

FIG. 35. Temperature distribution computed over a DPF segment with a unit temperature difference between the top and the other three sides (see Plate 11 in Color Plate Section at the end of this book).

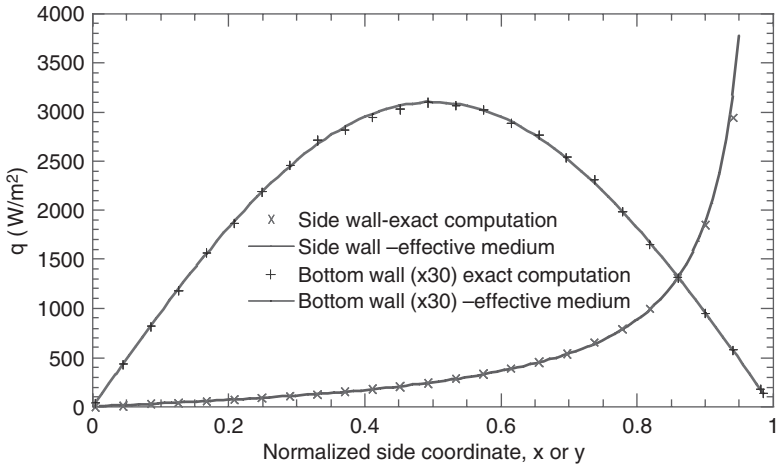

FIG. 36. Comparison between approximate and numerically computed heat fluxes on the two sides of a heated DPF segment with 24×24 channels.

the side of the unit cell. The approximation is very successful despite the singularity exhibited by the side flux close to the upper corner. Some inconsistencies are observed close to the singularity. This is expected due to the failure of the local averaging procedure in regions where the macroscopic rate of change of the flux is important on the scale of channel. The problem was also solved with the effective homogeneous medium theory with effective conductivity given by Eq. (38). The side length of the simulated segment is $L = 35\,\text{mm}$ and the ratio $w_s/(a + w_s)$ is 0.2. The fluxes from the homogeneous medium approximation shown in Fig. 36 are computed by:

$$\text{Side boundary} : \frac{q\ell}{\lambda_{t,\text{eff}}} = 4 \sum_{i=1,3,5\ldots}^{\infty} \frac{\sinh(i\pi y)}{\sinh(i\pi)} \tag{39}$$

$$\text{Bottom boundary} : \frac{q\ell}{\lambda_{t,\text{eff}}} = 4 \sum_{i=1,3,5\ldots}^{\infty} \frac{\sin(i\pi x)}{\sinh(i\pi)} \tag{40}$$

Having a validated model for the effective thermal conductivity of DPFs, it is possible to study segmented DPF designs. An example showing the influence of the segment's gluing material thermal conductivity on the inter-segment heat transfer is shown in Fig. 37.

B. MULTICHANNEL PHENOMENA

A single channel description is no longer applicable and the entire DPF needs to be simulated in case of no radially uniform inlet conditions to the trap.

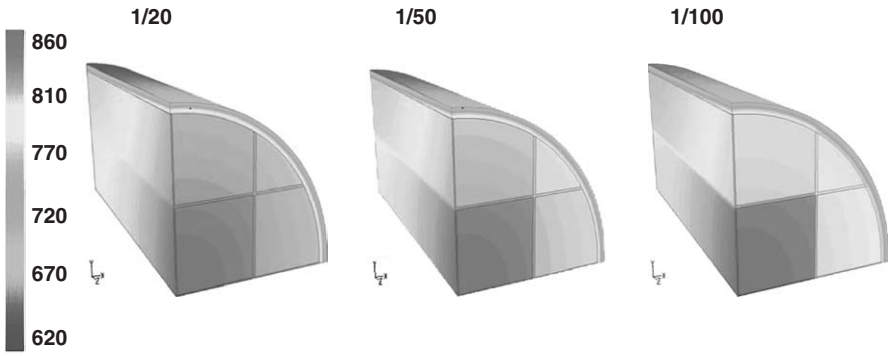

FIG. 37. Influence of the segment gluing material thermal conductivity to that of the segment (computed with the effective conductivity approach mentioned in the text) on the inter-segment heat transfer is shown (see Plate 12 in Color Plate Section at the end of this book).

A filter of realistic size consists of several thousand channels so its direct simulation via the numerical solution of a coupled discrete multichannel problem is an intractable task with the currently available computational resources. Alternatively the scale-up problem may be faced employing a continuum model of the filter honeycomb structure.

Rigorous scale homogenization procedures lead to continuum models for the entire DPF (Bissett, 1984; Konstandopoulos *et al.*, 2001, 2003); exploiting (as is common in continuum descriptions) a suitable scale disparity, namely the ratio of the channel hydraulic radius to the entire DPF diameter. The smallness of this parameter is invoked to formulate a perturbation expansion of the discrete multichannel equations. The continuum multichannel description of the DPF can accommodate various regeneration methods (thermal, catalytic and NO_2-assisted) and can provide spatio-temporal information of several quantities of interest (e.g. filter temperature, soot mass distribution, flow distribution, etc.) as illustrated in Fig. 38.

During incomplete regeneration radial non-uniformities might develop in a DPF as it was demonstrated in references Konstandopoulos *et al.* (2001, 2003). These non-uniformities will lead to flow redistribution during subsequent loading. A network analogy (Amador *et al.*, 2004) suggests itself as an obvious approximation to provide an alternative to CFD but we have not up to now evaluated its accuracy. We have to end this performed CFD calculations with Fluent of the flow distribution at the face of a DPF after incomplete regenerations leading to radial non-uniformities (Fig. 39) computed by a multichannel simulation (Konstandopoulos *et al.*, 2003) and these are compared to the flow distributions obtained from a network approximation in Fig. 40. The obtained flux-averaged error is 15% in the worst case. Current work is focusing on a composite network model, which employs a limited

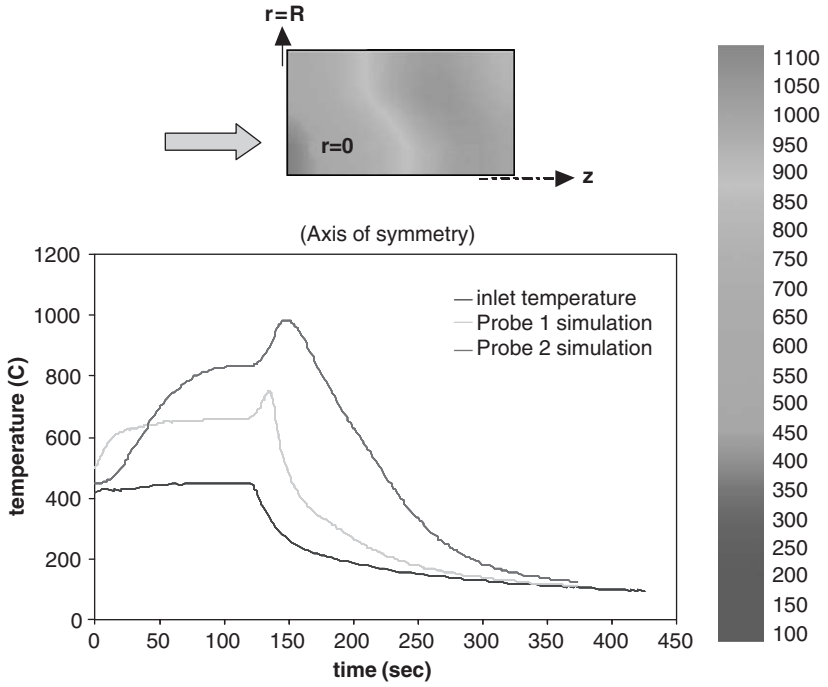

FIG. 38. Temporal evolution of temperature probes inserted in a regenerating DPF (bottom) along with the spatial distribution of filter temperature at 145 s, i.e. the moment of exothermic peak (top). Locations (r,z) in millimeter of temperature probes: Probe 1, (24.25,40) and Probe 2, (24.25,142) (see Plate 13 in Color Plate Section at the end of this book).

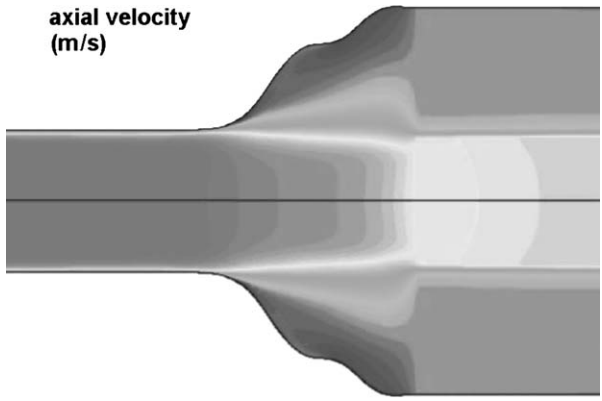

FIG. 39. Flow distribution at the entrance of a DPF with radially non-uniform soot distribution, resulting from incomplete regeneration (see Plate 14 in Color Plate Section at the end of this book).

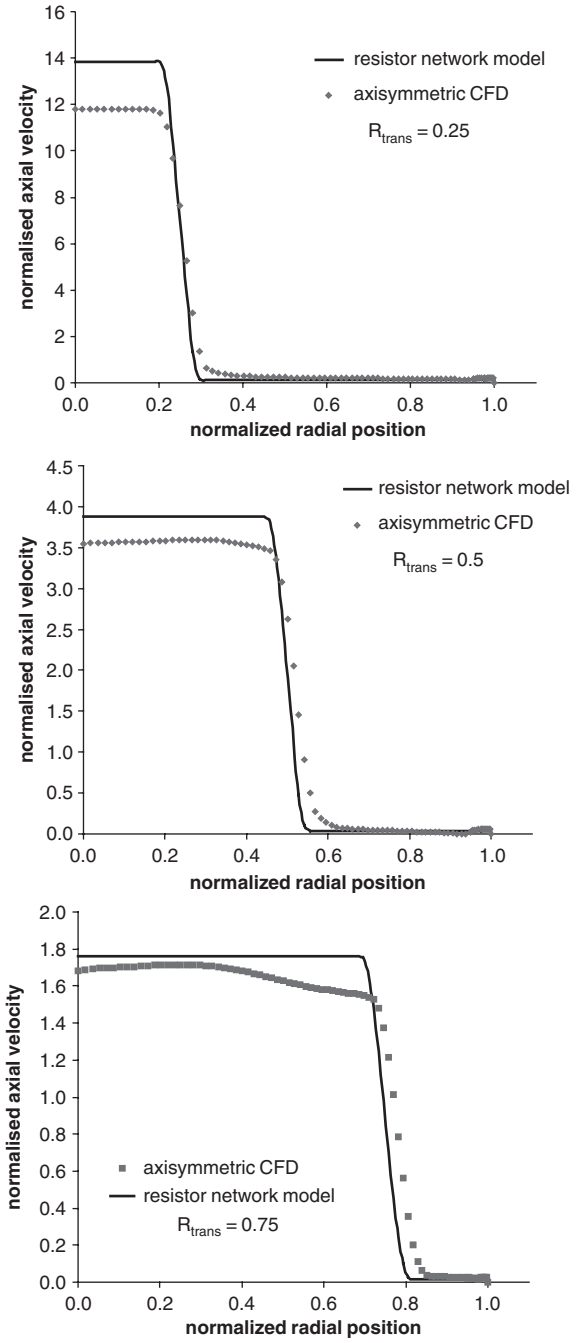

FIG. 40. Comparison of flow distribution at the entrance of a DPF with different radially non-uniform soot distributions computed by CFD and a simple network model.

amount of information from CFD simulation of an unloaded DPF to improve the above error figure.

The coupling of the DPF simulation to CFD appears inescapable in case of 3D flow distributions. We have interfaced our DPF multichannel model with Fluent employing the mechanism of user defined functions/subroutines. As an example of this coupling, we show in Fig. 41 the coupled CFD-multichannel simulation of a DPF placed downstream of a 45° bend in the exhaust. To make the simulation tractable the CFD solution is updated at every 0.5 gr increase of the filter soot load. From the snapshots of soot mass distribution and inlet velocity shown in Fig. 41 it becomes clear that the DPF inlet face velocity field moves in a self-regulated fashion toward a homogeneous distribution, while the soot mass distribution exhibits a stronger "memory" of the initial inlet distribution non-uniformity. An example of the DPF temperature field evolution during 3D simulation of regeneration is shown in Fig. 42.

As we proceed to the entire exhaust system scale we face the task of interfacing the DPF behavior to that of other emission control devices in the exhaust (e.g. diesel oxidation catalysts (DOC) and NO_x reduction devices). An example of a coupled simulation of a DOC and a DPF in series is shown in Fig. 43. We observe how a hydrocarbon pulse injection upstream of the DOC raises the exhaust temperature and causes regeneration of the DPF. Such simulation tools are very useful for the development and optimization of post-injection strategies for DPF regeneration.

Closing the section on the entire filter scale we may remark that at the multichannel level the dynamic ash model of Konstandopoulos *et al.* (2003) and Rodriguez-Perez *et al.* (2004) can reproduce ash deposition patterns occurring in fuel-additive assisted regeneration (Blanchard *et al.*, 2004) as seen in Fig. 44 as well as describe the pressure drop evolution due to ash accumulation as seen in Fig. 45.

VI. Conclusion

Experience has proven that a DPF should be treated as an integral part of the powertrain and that it requires a systemic approach for its optimal design and operation, the latter being matched to the engine management strategy. The identification of optimum combinations of emission control components by the process of hardware building and testing entire emission control system, often requires a prohibitive amount of man power and cost. In addition, deep knowledge of emission control component behavior is required to perform an effective system-level integration and optimization. Advanced computational tools are now recognized as tractable alternatives for the rapid assessment of various design options for a particular vehicle platform.

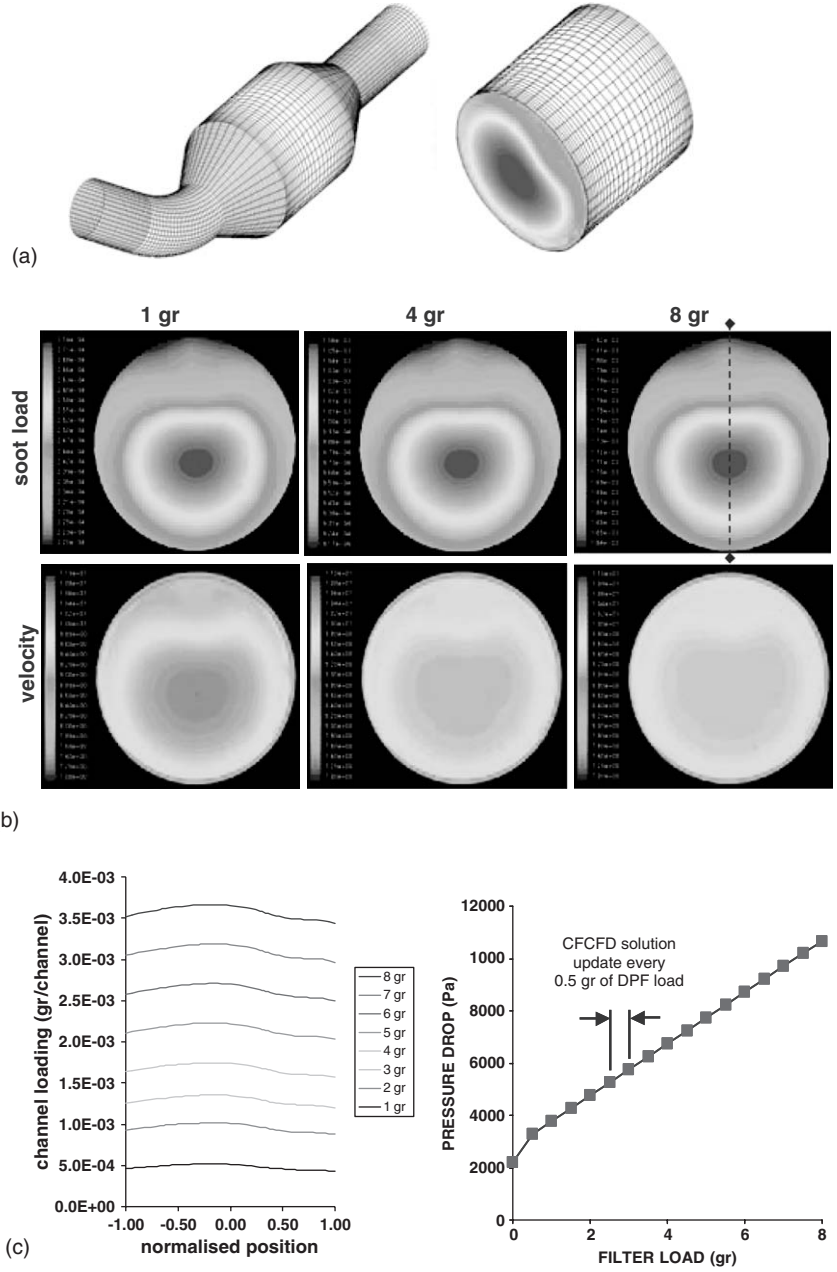

FIG. 41. (a) 3D simulation of a DPF placed downstream of a 45° bend in the exhaust. (b) Soot mass and velocity distribution at the inlet face at different soot loads of the filter. (c) Evolution of radial soot mass profile (along the dotted line) at different soot loads of the filter and resulting pressure drop (see Plate 15 in Color Plate Section at the end of this book).

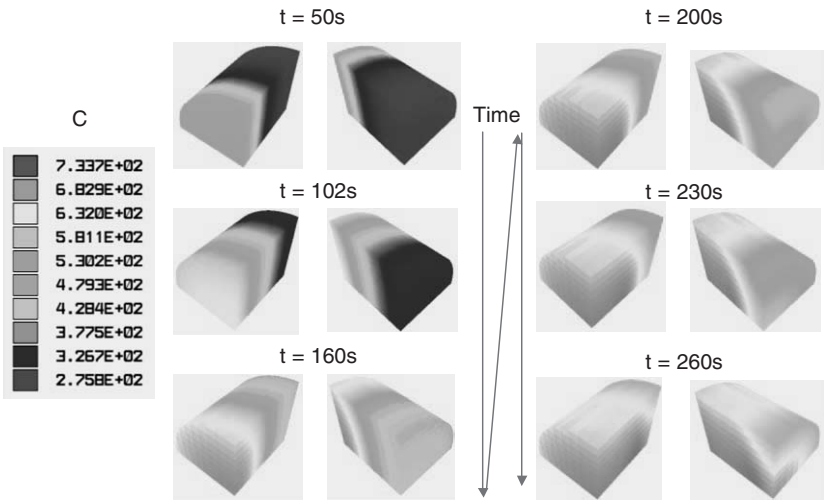

FIG. 42. 3D–DPF simulation. Example of temperature field evolution in a 11.25×12 in DPF during regeneration (see Plate 16 in Color Plate Section at the end of this book).

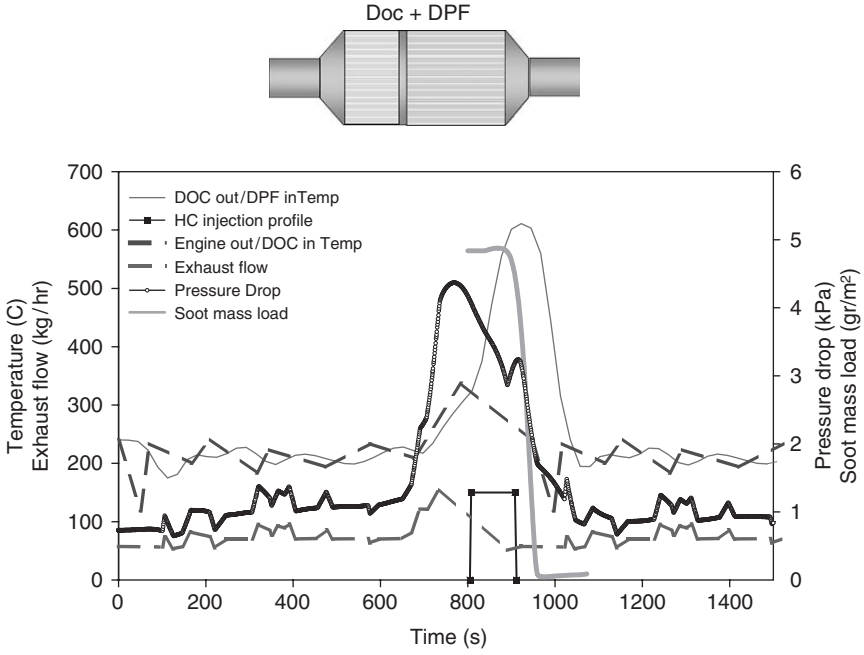

FIG. 43. Coupled DOC–DPF simulation. Filter regeneration by hydrocarbon injection upstream of the DOC over transient engine operation.

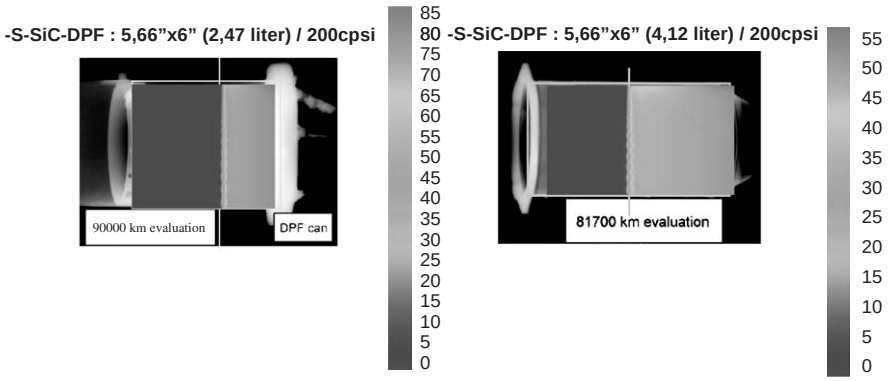

FIG. 44. Multichannel dynamic ash model. Simulation of additive ash accumulation at the end of the filter. Comparison with X-ray images of Blanchard *et al.* (2004) (see Plate 17 in Color Plate Section at the end of this book).

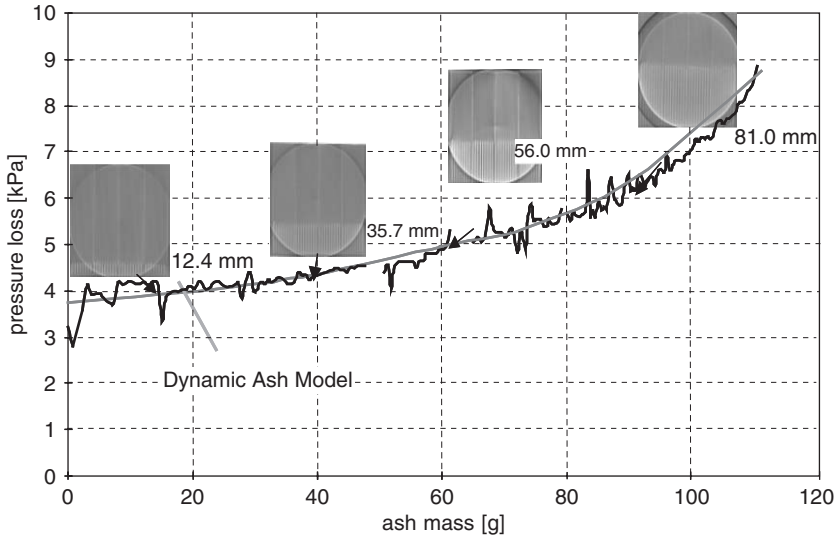

FIG. 45. Simulation of the effect of ash accumulation of pressure drop. The experimental data are courtesy of Ibiden Co. Ltd.

For basic filter material development wall scale models especially the MicroFlowS approach can be applied. During early development of particulate emission control systems single channel models provide a fast and sufficient means for basic DPF design and sizing analysis. In addition, when applicable

(i.e. in the absence of radial non-uniformities) they represent a valuable tool for analyzing experimental data collected under well-defined conditions and extraction of relevant physicochemical parameters of the system. Finally, detailed analysis and refinement of the selected DPF system can be achieved with the use of the multichannel models.

In the present chapter, we have outlined the current state of progress in DPF simulation drawing from our recent work in the area. Employing a convenient spatial scale classification of the various models we have provided a framework for the consistent integration of the information from the various models across all scales. While computing limitations still remain the barrier for the routine deployment of detailed simulations of coupled emission control components at the entire exhaust system scale, we anticipate that in the near future such simulations will be widely employed by the industry, exploiting grid-computing environments. This means that from a research point of view, DPF simulation will focus into providing a deeper understanding and more detailed description of the coupled transport, structural and reaction microphenomena occurring at the wall and pore scales, to materialize the vision for an *a priori* design of advanced microstructures, hosting multifunctional catalysts for the highly compact and efficient emission control devices of the future.

NOMENCLATURE

a	side length of channel cross section
c_{pg}	specific heat capacity of exhaust gas
c_{ps}	specific heat capacity of soot
c_{pw}	specific heat capacity of filter wall material
d_c	grain diameter
d_{pr}	soot primary particle size
E_{cat}	activation energy for catalytic soot oxidation
E'_f	parameter in catalytic CO selectivity Eq. (11)
E_f	parameter in thermal CO selectivity Eq. (5)
E_{th}	activation energy for thermal soot oxidation
f_{CO}^{cat}	catalytic CO selectivity
f_{CO}^{th}	thermal CO selectivity
G	exhaust mass flux (with respect to filtration area)
F_{ox}	local soot oxidation rate
k	permeability
k_1	volumetric reaction constant for soot oxidation with NO_2
k'_A,k_B	forward and reverse volumetric reaction constants for NO oxidation
k_A	modified forward volumetric reaction constant for NO oxidation
K_{cat}	rate coefficient of catalytic soot oxidation

k'_f	parameter in catalytic CO selectivity equation
k_f	parameter in thermal CO selectivity equation
$k_{o,\mathrm{cat}}$	preexponential factor for catalytic soot oxidation
$k_{o,\mathrm{th}}$	preexponential factor for thermal soot oxidation
K_{th}	rate coefficient of thermal soot oxidation
k_{soot}	soot permeability
k_{wall}	wall permeability
ℓ	length of segment size
L	slit half width
M_{c}	molecular weight of soot
M_{CO}	molecular weight of CO
$M_{\mathrm{CO_2}}$	molecular weight of CO_2
M_{ox}	molecular weight of oxygen
m_{w}	filter wall mass per unit filtration area
m_{i}	soot mass in layer i
Pe_{T}	thermal Peclet number for gas $u_{\mathrm{w}}a/\alpha_{\mathrm{th}}$
q	local heat flux
Re_{w}	wall Reynolds number au_{w}/v
R_{g}	ideal gas density
R	recycling factor for soot oxidation by NO
S	specific surface area (per unit mass) of soot layer
T_{c}	channel cup mixing temperature
T_o	filter and gas temperature at $t=0$
$\overline{u}_z$	mean axial channel velocity
u_{w}	superficial filtration velocity
w	soot layer thickness
w_{s}	filter wall thickness
X,Y,Z	molar concentration of NO_2, NO and total NO_x respectively (Appendix).
y	oxygen molar fraction in exhaust gases
Y	oxygen mass fraction in exhaust gases
Y_{CO}	CO mass fraction in exhaust gases
$Y_{\mathrm{CO_2}}$	CO_2 mass fraction in exhaust gases

GREEK LETTERS

α, γ	generalized soot layer structural descriptors
α_{th}	thermal diffusivity of the gas
β	index for the completeness of soot oxidation (Appendix), Forchheimer coefficient (Eqs. 1 and 3)
ΔH	heat of soot oxidation reaction (per unit mass of soot)
ΔH_{CO}	specific heat of CO formation
$\Delta H_{\mathrm{CO_2}}$	specific heat of CO_2 formation

ε	wall porosity
ε_A	open area fraction
θ	parameter in thermal CO selectivity equation
θ'	parameter in catalytic CO selectivity equation
$\lambda_{a,eff}$	effective axial thermal conductivity of the filter
$\lambda_{t,eff}$	effective radial thermal conductivity of the filter
λ_w	wall thermal conductivity
ν	kinematic viscosity of the gas
μ	gas viscosity
ρ	soot layer density
$\tilde{\rho}$	intrinsic soot density
ρ_g	exhaust gas density
τ	dimensionless time
ϕ	solid fraction in the deposit

-Subscript *o* denotes the initial value
-Overbar denotes dimensionless quantity
-O() denotes "on the order of"

ABBREVIATIONS

1, 2, 3D	one, two, three dimensional
CAST	combustion aerosol standard
CFD	computational fluid dynamics
DOC	diesel oxidation catalyst
DPF	diesel particulate filter
ECU	engine control unit
LNC	lean NO_X converter
LNT	lean NO_X trap
OAF	open area fraction
ODE	ordinary differential equations
SCR	selective catalytic reduction
SEM	scanning electron microscope
SMPS	scanning mobility particle sizer

ACKNOWLEDGMENTS

This work has been supported in part by the European Commission through the (ART-, PSICO-, SYLOC-, STYFF-) DEXA cluster projects as well as projects COMET, IMITEC and FLOWGRID. An earlier account of this work has been presented in the 2005 SAE World Congress. We thank Dr. E. Kikkinides for sharing his expertise on porous media reconstruction and

Mr. A. Tsakis for his assistance with computations. We are also thankful to all of our colleagues at the APT Lab for their support in carrying out the work presented. Ibiden Co. Ltd. Japan is acknowledged for providing the experimental data in Fig. 45.

REFERENCES

Amador, C., Gavriilidis, A., and Angeli, P. *Chem. Eng. J.* **101**(1–3), 379–390 (2004).

Bardasz, E., Mackney, D., Britton, N., Kleinschek, G., Olofsson, K., Murray, I., and Walker, A. P. Investigations of the interactions between lubricant-derived species and aftertreatment systems on a state-of-the-art heavy duty diesel engine. SAE Technical Paper No. 2003-01-1963 (2003).

Bardon, S., Bouteiller, B., Bonnail, N., Girot, P., Gleize, V., Oxarango, L., Higelin, P., Michelin, J., Schuerholz, S., and Terres, F. Asymmetrical channels to increase DPF lifetime. SAE Technical Paper No. 2004-01-0950 (2004).

Bissett, E. J. *Chem. Eng. Sci.* **39**(7/8), 1233–1244 (1984).

Bissett, E. J., and Shadman, F. *AIChE J.* **31**(5), 753–758 (1985).

Blanchard, G., Colignon, C., Griard, C., Rigaudeau, C., Salvat, O., and Seguelong, T. Passenger car series application of a new diesel particulate filter system using a new ceria-based, fuel-borne catalyst: from the engine test bench to European vehicle certification. SAE Technical Paper No. 2002-01-2781 (2004).

Boretto, G., Imarisio, R., Rellecati, P., Barucchi, E., and Sanguedolce, A. ''Serial Application of a Catalyzed Particulate Filter on Common Rail DI Diesel Engines For Passenger Cars.'' F2004V068, FISITA World Automotive Congress, Barcelona, Spain, 2004, May 23–27.

Chen, S., and Doolen, G. *Ann. Rev. Fluid Mech.* **30**, 329 (1998).

Dardiotis, C. K., Haralampous, O. A., and Koltsakis, G. C. *Ind. Eng. Chem. Res.* **45**, 3520–3530 (2006).

Dullien, F. A. L., ''Porous Media''. Academic Press Inc, San Diego (1979).

Fluent Inc. Fluent 6 User's Guide, December (2001).

Gropi, G., and Tronconi, E. *AIChE. J.* **42**(8), 2382–2387 (1996).

Hawker, P., Myers, N., Huthwohl, G., Vogel, H., Bates, B., Magnusson, L., and Bronneberg, P. Experience with a new particulate trap technology in Europe. SAE Paper No 970182, (1997).

http://www.unizar.es/flowgrid/

Hwang, G. J., Cheng, Y. C., and Ng, M. L. *Int. J. Heat Mass Transfer* **36**, 2429–2440 (1990).

Jacquot, F., Logie, V., Brilhac, J. F., and Gilot, P. *Carbon* **40**(3), 335–343 (2002); See also, Setiabudi, A., Makkee, M., and Moulijn, J. A. *Appl. Catal. B: Environ.* **50**(3), 185–194 (2002).

Johnson, T. V. Diesel emission control technology-2003 in review. SAE Technical Paper No. 2004-01-0070 (2004).

Karadimitra, K., Lorentzou, S., Agrafiotis C., and Konstandopoulos A. G. ''Modeling of Catalytic Particle Synthesis via Spray Pyrolysis & In-Situ Deposition on Porous Materials''. PARTEC 2004, International Conference for Particle Technology, Nuremberg, Germany, 2004, March 16–18.

Kikkinides, E. S., and Burganos, V. N. *Phys. Rev. E* **62**(5), 6906 (2000).

Kinney, R. B. *Int. J. Heat Mass Transfer* **11**, 1393–1401 (1968).

Knoth, J. F., Drochner, A., Vogel, H., Gieshoff, J., Kögel, M., Pfeifer, M., and Votsmeier, M. *Catal. Today* **105**, 598–604 (2005); See also, Votsmeier, M., Gieshoff, J., Kögel, M., Pfeifer, M., Knoth, J. F., Drochner, A., and Vogel, H. ''Wall-flow filters with wall-integrated oxidation catalyst: A simulation study'' *Appl. Catal. B: Environ.*, in press, Corrected Proof, Available online 28 July 2006.

Konstandopoulos, A. G. *Powder Tech.* **109**(1–3), 262–277 (2000).
Konstandopoulos, A. G. Flow resistance descriptors for diesel particulate filters: Definitions, measurements and testing. SAE Technical Paper No. 2003-01-0846 (SP-1755) (2003).
Konstandopoulos, A. G. "Convective-diffusive deposition of fractal-like aggregates and the microstructure and properties of the resulting nanostructured deposits" (to be submitted) (2007).
Konstandopoulos, A. G., and Johnson, J. H. Wall-flow diesel particulate filters-their pressure drop and collection efficiency. SAE Technical Paper No. 890405, SAE Trans. 98 sec. 3 (J. Engines), pp. 625–647 (1989).
Konstandopoulos, A. G., and Kladopoulou, E. "A Virtual Sensor for On-board Diagnostics and Control of Diesel Particulate Filters". CDAuto03A2028, CD AUTO 03, *4th International Conference on Control and Diagnostics in Automotive Applications*, Sestri-Levante, Italy, 2003, June 18–20.
Konstandopoulos, A. G., and Kladopoulou, E. The optimum cell density for wall-flow monolithic filters: Effects of filter permeability, soot cake structure and ash loading. SAE Technical Paper No. 2004-01-1133 (2004).
Konstandopoulos, A. G., and Kostoglou, M. "A mathematical model of soot oxidation on catalytically coated ceramic filters". Advances in Vehicle Control and Safety (AVCS'98), Amiens, France, July 1–3, 1998.
Konstandopoulos, A. G., and Kostoglou, M. "Theory and Practice of Soot Filter Operation". Proceedings of Global Powertrain Congress 99 (invited paper), Powertrain Int., Stuttgart, 1999a, October 5–7.
Konstandopoulos, A. G., and Kostoglou, M. Periodically reversed flow regeneration of diesel particulate traps. SAE Technical Paper No. 1999-01-0469 (1999b).
Konstandopoulos, A. G., and Kostoglou, M. *Combust. Flame* **121**(3), 488–500 (2000).
Konstandopoulos, A. G., and Kostoglou, M. Microstructural aspects of soot oxidation in diesel particulate filters. SAE Technical Paper No. 2004-01-0693 (SP-1861) (2004).
Konstandopoulos, A. G., Kostoglou, M., and Housiada, P. Spatial non-uniformities in diesel particulate trap regeneration. SAE Technical Paper No. 2001-01-0908 (SP-1582) (2001).
Konstandopoulos, A. G., Kostoglou, M., Housiada, P., Vlachos, N., and Zarvalis, D. Multichannel simulation of soot oxidation in diesel particulate filters. SAE Technical Paper No. 2003-01-0839 (2003).
Konstandopoulos, A. G., Kostoglou, M., Skaperdas, E., Papaioannou, E., Zarvalis, D., and Kladopoulou, E., Fundamental studies of diesel particulate filters: Transient loading, regeneration and aging. SAE Technical Paper No. 2000-01-1016 (SP-1497) (2000).
Konstandopoulos, A. G., Lorentzou, S., and Kostoglou, M. Wall scale reaction models in diesel particulate filters. SAE Technical Paper No. 2007-1-1130 (2007).
Konstandopoulos, A. G., Skaperdas, E., and Masoudi, M. Inertial contributions to the pressure drop of diesel particulate filters. SAE Technical Paper No. 2001-01-0909 (SP-1582) (2001).
Konstandopoulos, A. G., Skaperdas, E., and Masoudi, M. Microstructural properties of soot deposits in diesel particulate traps. SAE Technical Paper No. 2002-01-1015 (SP-1673) (2002).
Konstandopoulos, A. G., Skaperdas, E., Warren, J., and Allanson, R. Optimized filter design and selection criteria for continuously regenerating diesel particulate traps. SAE Technical Paper No. 1999-01-0468 (1999).
Konstandopoulos, A. G., Vlachos, N., Housiada, P., and Kostoglou, M. Simulation of triangular-cell-shaped, fibrous wall-flow filters. SAE Technical Paper No. 2003-01-0844 (SP-1755) (2003).
Konstandopoulos, A. G., Vlachos, N., Stavropoulos, I., Skopa, S., Schumacher, U., and Woiki, D. Study of a sintered metal diesel particulate trap. SAE Technical Paper Offer No. 05FL-106, (submitted) (2005).
Konstandopoulos, A. G., Zarvalis, D., Papaioannou, E., Vlachos, N. D., Boretto, G., Pidria, M. F., Faraldi, P., Piacenza, O., Prenninger, P., Cartus, T., Schreier, H., Brandstatter, W., Wassermayr, C., Lepperhof, G., Scholz, V., Luers, B., Schnitzler, J., Claussen, M.,

Wollmann, A., Maly, M., Tsotridis, G., Vaglieco, B. M., Merola, S. S., Webster, D., Bergeal, D., Gorsmann, C., Obernosterer, H., Fino, D., Russo, N., Saracco, G., Specchia, V., Moral, N., D'Anna, A., D'Alessio, A., Zahoransky, R., Laile, E., Schmidt, S., and Ranalli, M. The diesel exhaust aftertreatment (DEXA) cluster: A systematic approach to diesel particulate emission control in Europe. SAE Technical Paper No. 2004-01-0694 (SP-1861) (2004).

Kostoglou, M., Housiada, P., and Konstandopoulos, A. G. *Chem. Eng. Sci.* **58**, 3273–3283 (2003).

Lueders, H., Stommel, P., and Geckler, S. Diesel exhaust treatment-new approaches to ultra low emission diesel vehicles. SAE Paper No. 1999-01-0108 (1999).

Muntean, M., Rector, D., Herling, D., Khaleel, M., and Lessor, D. Lattice-Boltzmann diesel particulate filter sub-grid modelling-a progress report. SAE Technical Paper No. 2003-01-0835 (2003).

Nakatani, K., Hirota, S., Takeshima, S., Itoh, K., Tanaka, T., and Dohmae, K. Simultaneous PM and NO_x reduction system for diesel engines. SAE Technical Paper No. 2002-01-0957 (2002).

Ogyu, K., Ohno, K., Hong, S., and Komori, T. Ash storage capacity enhancement of diesel particulate filter. SAE Technical Paper No. 2004-01-0949 (2004).

Olsson, L., Persson, H., Fridell, E., Skoglundh, M., and Andersson, B. *J. Phys. Chem. B* **105**(29), 6895–6906 (2001); See also, Olsson, L., Westerberg, B., Persson, H., Fridell, E., Skoglundh, M., and Andersson, B. *J. Phys. Chem. B* **105**, 10433–10439 (2001).

Peters, B. Integrated 1d to 3d simulation workflow of exhaust aftertreatment devices. SAE Technical Paper No. 2004-01-1132 (2004).

Raithby, G. *Int. J. Heat Mass Transfer* **14**, 223–243 (1971).

Rodriguez-Perez, D., Castillo, J. L., Antoranz, J. C., Konstandopoulos, A. G., and Vlachos, N. "Mixed ODE-MC Model for the Soot Cake Formation in a Square Section Filter". European Aerosol Conference EAC 2004, Budapest, Hungary, 2004, September 6–10.

SAE International. Diesel exhaust emission control, SP-1860, ISBN 0-7680-1396-8 (2004).

Skaperdas, E., and Konstandopoulos, A. G. "Prediction of Diesel Particulate Filter Loading Behavior for System Control Applications", CD AUTO 01, 3rd International Conference on Control and Diagnostics in Automotive Applications, Sestri-Levante, Italy, 2001, July 4–6.

Tassopoulos, M. "Relationships between particle deposition mechanism, deposit microstructure and effective transport properties". PhD Thesis, Yale University, USA (1991).

Tomadakis, M. M., and Sotirchos, S. V. *AIChE J.* **37**, 1175 (1991a).

Tomadakis, M. M., and Sotirchos, S. V. *AIChE J.* **37**, 74 (1991b).

Torquato, S., "Random Heterogeneous Materials: Microstructure and Macroscopic Properties". Springer, New York (2001).

Vlachos, N., Housiada, P., Zarvalis, D., and Konstandopoulos, A. G., Transient filtration and pressure drop behavior of diesel particulate filters, *in* "Particle Loading and Kinetics of Filtration in Fibrous Filters" (M. J. Lehmann, and G. Kasper Eds.), pp. 13–26. University of Karlsruhe, Karlsruhe (2002).

Young, D. M., Hickman, D. L., Bhatia, G., and Gunasekaran, N. Ash storage concept for diesel particulate filters. SAE Technical Paper No. 2004-01-0948 (2004).

Zarvalis, D., Altiparmakis, C., Mei, F., and Konstandopoulos, A. G. "Evaluation of a Multi-layer Sintered Metal Fibrous Diesel Particulate Filter". European Aerosol Conference EAC 2003, Madrid, Spain, 2003, August 31–September 5.

Appendix. Microstructural Model of Soot Oxidation: The Effect of Catalyst

In the two-layer model of a catalytic coating, soot particles oxidize when found within the "field of catalyst action". This is modeled with a parameter

β denoting the fraction (0–1) of the soot surface in "contact" with the catalyst (meaning within its field of action) and in principle it depends on coating structure and amount of soot loading of the filter. In the present model the parameter β is taken as a constant although in principle can vary dynamically due to soot deposition conditions and/or flow or reaction induced restructuring of the soot. The layer can "store" a certain amount of soot until it is filled-up, which depends on coating structure and filtration velocity. The remaining soot particles form a "queue" on top of the filled-up catalyst-influenced layer, and this second layer can be oxidized only thermally.

In the presence of a catalyst and with a finite selectivity for CO production, soot oxidation is described with the following global reactions, one for the thermal and one for the catalytic path (i.e. oxidation of soot by oxygen transferred from the catalyst by a redox and/or spill-over mechanism). Konstandopoulos and Kostoglou (1999b, 2000):

$$\mathrm{C} + (1 - f_{\mathrm{CO}}^{\mathrm{th}}/2)\mathrm{O}_2 \rightarrow f_{\mathrm{CO}}^{\mathrm{th}}\mathrm{CO} + (1 - f_{\mathrm{CO}}^{\mathrm{th}})\mathrm{CO}_2 \tag{41}$$

$$\mathrm{C} + (1 - f_{\mathrm{CO}}^{\mathrm{cat}}/2)\mathrm{O}_2 \rightarrow f_{\mathrm{CO}}^{\mathrm{cat}}\mathrm{CO} + (1 - f_{\mathrm{CO}}^{\mathrm{cat}})\mathrm{CO}_2 \tag{42}$$

The local soot oxidation rate is

$$F_{\mathrm{ox}} = -[(1-\beta)K_{\mathrm{th}} + \beta K_{\mathrm{cat}})]S\rho_{\mathrm{g}}\rho\, Y\frac{M_{\mathrm{c}}}{M_{\mathrm{ox}}} \tag{43}$$

The conservation equations for the different species across the soot layer are

$$u_{\mathrm{w}}\frac{\mathrm{d}Y}{\mathrm{d}x} = [(1 - f_{\mathrm{CO}}^{\mathrm{th}}/2)(1-\beta)K_{\mathrm{th}} + (1 - f_{\mathrm{CO}}^{\mathrm{cat}}/2)\beta K_{\mathrm{cat}})]S\rho\, Y \tag{44}$$

$$u_{\mathrm{w}}\frac{\mathrm{d}Y_{\mathrm{CO}}}{\mathrm{d}x} = [f_{\mathrm{CO}}^{\mathrm{th}}(1-\beta)K_{\mathrm{th}} + f_{\mathrm{CO}}^{\mathrm{cat}}\beta K_{\mathrm{cat}}]S\rho\, Y\frac{M_{\mathrm{CO}}}{M_{\mathrm{ox}}} \tag{45}$$

$$u_{\mathrm{w}}\frac{\mathrm{d}Y_{\mathrm{CO_2}}}{\mathrm{d}x} = [(1 - f_{\mathrm{CO}}^{\mathrm{th}})(1-\beta)K_{\mathrm{th}} + (1 - f_{\mathrm{CO}}^{\mathrm{cat}})\beta K_{\mathrm{cat}}]S\rho\, Y\frac{M_{\mathrm{CO_2}}}{M_{\mathrm{ox}}} \tag{46}$$

A total mass balance for O_2 gives:

$$Y(0) - Y(w) = \frac{1}{2}\frac{M_{\mathrm{ox}}}{M_{\mathrm{CO}}}Y_{\mathrm{CO}}(w) + \frac{M_{\mathrm{ox}}}{M_{\mathrm{CO_2}}}Y_{\mathrm{CO_2}}(w) \tag{47}$$

The initial conditions for the above equations are:

$$\text{at } x = w: \; Y = Y_{\text{in}}(t), \quad Y_{\text{co}} = Y_{\text{co}_2} = 0 \tag{48}$$

The deposit evolution equations according to the microstructural model introduced in Konstandopoulos and Kostoglou (2004) with parameters α and γ are:

$$\frac{\partial \rho}{\partial t} = \alpha F_{\text{ox}} - \dot{x}\frac{\partial \rho}{\partial x} \tag{49}$$

$$\dot{x} = \int_0^x (1-\alpha)\frac{F_{\text{ox}}}{\rho}\,\mathrm{d}z \tag{50}$$

$$\frac{S}{S_o} = \left(\frac{\rho_o}{\rho}\right)^{\gamma} \tag{51}$$

$$(c_{\text{pw}} m_{\text{w}} + c_{\text{ps}} M)\frac{\mathrm{d}T}{\mathrm{d}t} = \Delta H_{\text{CO}} G Y_{\text{CO}}(w)\frac{M_{\text{c}}}{M_{\text{CO}}} + \Delta H_{\text{CO}_2} G Y_{\text{CO}_2}(w)\frac{M_{\text{c}}}{M_{\text{CO}_2}} + G c_{\text{pg}}(T_{\text{in}} - T) \tag{52}$$

where

$$K_{\text{th}} = k_{o,\text{th}} T \mathrm{e}^{-(E_{\text{th}}/R_{\text{g}}T)} \tag{53}$$

$$K_{\text{cat}} = k_{o,\text{cat}} T \mathrm{e}^{-(E_{\text{cat}}/R_{\text{g}}T)} \tag{54}$$

$$f_{\text{CO}}^{\text{th}} = \frac{1}{1 + k_f y^{\theta} \mathrm{e}^{E_f/R_{\text{g}}T}} \tag{55}$$

$$f_{\text{CO}}^{\text{cat}} = \frac{1}{1 + k'_f y^{\theta'} \mathrm{e}^{E'_f/R_{\text{g}}T}} \tag{56}$$

The following dimensionless variables are introduced:

$$\overline{T} = T/T_o, \quad \overline{Y} = Y/Y_o, \quad \overline{Y}_{\text{CO}} = Y_{\text{CO}}/Y_o$$

$$\overline{Y}_{\text{CO}_2} = Y_{\text{CO}_2}/Y_o, \quad \overline{G} = G/G_o, \quad \overline{M} = M/M_o$$

$$\rho = \rho/\rho_o, \quad \overline{S} = S/S_o, \quad \overline{x} = x/w_o$$

$$\overline{w} = w/w_o, \quad \overline{\rho}_g = \rho_g/\rho_{go},$$

$$\overline{K}_{th} = \frac{K_{th}}{K_o}, \quad \overline{K}_{cat} = \frac{K_{cat}}{K_o}, \quad A = \frac{K_o w_o \rho_o S_o}{u_w}$$

$$\tau = \frac{M_c}{M_{ox}} T_o S_o \rho_{go} Y_o$$

$$C_{1A} = \frac{G_o \Delta H_{CO}}{c_{pw} m_w T_o K_o S_o \rho_{go}} \frac{M_{CO}}{M_c}$$

$$C_{1B} = \frac{G_o \Delta H_{CO_2}}{c_{pw} m_w T_o K_o S_o \rho_{go}} \frac{M_{CO_2}}{M_c}$$

$$C_2 = \frac{M_{ox} G_o c_{pg}}{M_c c_{pw} m_w K(T_o) S_o \rho_{go} Y_o}$$

$$C_3 = \frac{c_{ps} M_o}{c_{pw} m_w}$$

where T_o is the initial filter temperature, Y_o the inlet oxygen mass fraction at $t=0$, G_o the exhaust mass flux (with respect to filtration area) at $t=0$, M_o the initial soot mass per unit filtration area, ρ_{go} the exhaust density at $t=0$ (from the ideal gas law) and ρ_o and S_o are reference values for the density and surface area of the deposit, respectively. Using the new variables, the Lagrangian form of the problem that must be solved is

$$\frac{d\overline{Y}}{d\overline{x}} = \frac{1}{\overline{G}(\tau)\overline{T}}[(1 - f_{CO}^{th}/2)(1-\beta)\overline{K}_{th} + (1 - f_{CO}^{cat}/2)\beta\overline{K}_{cat})]A\overline{\rho}^{1-\gamma}\overline{Y} \tag{57}$$

$$\frac{d\overline{Y}_{CO}}{d\overline{x}} = \frac{1}{\overline{G}(\tau)\overline{T}} \frac{M_{CO}}{M_{ox}}[f_{CO}^{th}(1-\beta)\overline{K}_{th} + f_{CO}^{cat}\beta\overline{K}_{cat})]A\overline{\rho}^{1-\gamma}\overline{Y} \tag{58}$$

$$\frac{d\overline{Y}_{CO_2}}{d\overline{x}} = \frac{1}{\overline{G}(\tau)\overline{T}} \frac{M_{CO_2}}{M_{ox}}[(1 - f_{CO}^{th})(1-\beta)\overline{K}_{th} + (1 - f_{CO}^{cat})\beta\overline{K}_{cat})]A\overline{\rho}^{1-\gamma}\overline{Y} \tag{59}$$

$$\frac{d\overline{\rho}}{d\tau} = -\alpha\frac{1}{\overline{T}}[(1-\beta)\overline{K}_{th} + \beta\overline{K}_{cat}]\overline{\rho}^{1-\gamma}\overline{Y} \tag{60}$$

$$\frac{\mathrm{d}\overline{x}}{\mathrm{d}\tau} = -\frac{(1-\alpha)}{\overline{T}} \int_0^{\overline{x}} [(1-\beta)\overline{K}_{\mathrm{th}} + \beta\overline{K}_{\mathrm{cat}}]\overline{\rho}^{-\gamma}\overline{Y}\mathrm{d}z \tag{61}$$

$$(1 + C_3\overline{M})\frac{\mathrm{d}\overline{T}}{\mathrm{d}\tau} = \overline{G}(\tau)(C_{1\mathrm{A}}\overline{Y}_{\mathrm{CO}}(w) + C_{1\mathrm{B}}\overline{Y}_{\mathrm{CO_2}}(w)) + C_2\overline{G}(\tau)(\overline{T}_{\mathrm{in}}(\tau) - \overline{T}) \tag{62}$$

with initial and boundary conditions

$$\overline{Y} = \overline{Y}_{\mathrm{in}}(t) \quad \text{at} \quad \overline{x} = \overline{w} \tag{63}$$

$$\overline{\rho}(x, 0) = \overline{\rho}_o(\overline{x}) \tag{64}$$

$$\overline{T}(0) = 1 \tag{65}$$

The above system is discretized across the soot layer leading to the following set of ordinary differential equations

$$\begin{aligned}\overline{Y}_i = \exp[-A\frac{1}{\overline{G}\,\overline{T}}\frac{1}{2}\sum_{j=i+1}^{L}(((1 - f_{\mathrm{CO}}^{\mathrm{th}}(\overline{Y}_i)/2)(1-\beta_j)\overline{K}_{\mathrm{th}} \\ + (1 - f_{\mathrm{CO}}^{\mathrm{cat}}(\overline{Y}_i)/2)\beta_j K_{\mathrm{cat}})\overline{\rho}_j^{1-\gamma} + ((1 - f_{\mathrm{CO}}^{\mathrm{th}}(\overline{Y}_{i-1})/2)(1-\beta_{j-1})\overline{K}_{\mathrm{th}} \\ + (1 - f_{\mathrm{CO}}^{\mathrm{cat}}(\overline{Y}_{i-1})/2)\beta_{j-1}K_{\mathrm{cat}})\overline{\rho}_{j-1}^{1-\gamma})(x_j - x_{j-1})]\end{aligned} \tag{66}$$

$$\frac{\mathrm{d}\overline{\rho}_i}{\mathrm{d}\tau} = -\alpha\frac{1}{\overline{T}}((1-\beta_i)\overline{K}_{\mathrm{th}} + \beta_i\overline{K}_{\mathrm{cat}})\overline{\rho}_i^{1-\gamma}\overline{Y}_i \tag{67}$$

$$\begin{aligned}\frac{\mathrm{d}\overline{x}_i}{\mathrm{d}\tau} = -(1-\alpha)\frac{1}{2\overline{T}}\sum_{j=i+1}^{L}(((1-\beta_j)\overline{K}_{\mathrm{th}} + \beta_j\overline{K}_{\mathrm{cat}})\overline{\rho}_j^{-\gamma}\overline{Y}_j \\ + ((1-\beta_{j-1})\overline{K}_{\mathrm{th}} + \beta_{j-1}\overline{K}_{\mathrm{cat}})\overline{\rho}_{j-1}^{-\gamma}\overline{Y}_{j-1})(x_j - x_{j-1})\end{aligned} \tag{68}$$

$$\begin{aligned}\overline{Y}_{\mathrm{CO},i} = A\frac{1}{\overline{G}\,\overline{T}}\frac{1}{2}\sum_{j=i+1}^{L}[((f_{\mathrm{CO}}^{\mathrm{th}}(\overline{Y}_i)(1-\beta_j)\overline{K}_{\mathrm{th}} \\ + f_{\mathrm{CO}}^{\mathrm{cat}}(\overline{Y}_i)\beta_j K_{\mathrm{cat}})\overline{\rho}_j^{1-\gamma}\overline{Y}_j + (f_{\mathrm{CO}}^{\mathrm{th}}(\overline{Y}_{i-1})(1-\beta_{j-1})\overline{K}_{\mathrm{th}} \\ + f_{\mathrm{CO}}^{\mathrm{cat}}(\overline{Y}_{i-1})\beta_{j-1}K_{\mathrm{cat}})\overline{\rho}_{j-1}^{1-\gamma}\overline{Y}_{j-1})(x_j - x_{j-1})]\frac{M_{\mathrm{CO}}}{M_{\mathrm{ox}}}\end{aligned} \tag{69}$$

$$\overline{Y}_{\mathrm{CO}_2,i} = A\frac{1}{\overline{G}\,\overline{T}}\frac{1}{2}\sum_{j=i+1}^{L}[((((1-f_{\mathrm{CO}}^{\mathrm{th}}(\overline{Y}_i))(1-\beta_j)\overline{K}_{\mathrm{th}} + (1-f_{\mathrm{CO}}^{\mathrm{cat}}(\overline{Y}_i))\beta_j K_{\mathrm{cat}})\overline{\rho}_j^{1-\gamma}\overline{Y}_j + (1-f_{\mathrm{CO}}^{\mathrm{th}}(\overline{Y}_{i-1}))(1-\beta_{j-1})\overline{K}_{\mathrm{th}} + (1-f_{\mathrm{CO}}^{\mathrm{cat}}(\overline{Y}_{i-1}))\beta_{j-1}K_{\mathrm{cat}})\overline{\rho}_{j-1}^{1-\gamma}\overline{Y}_{j-1})(x_j - x_{j-1})]\frac{M_{\mathrm{CO}_2}}{M_{\mathrm{ox}}} \tag{70}$$

where $x_i(0) = x_{io}$ are the initial grid points. Each time the density in a grid point becomes zero, this grid point is eliminated and the ODE integrator is reinitialized.

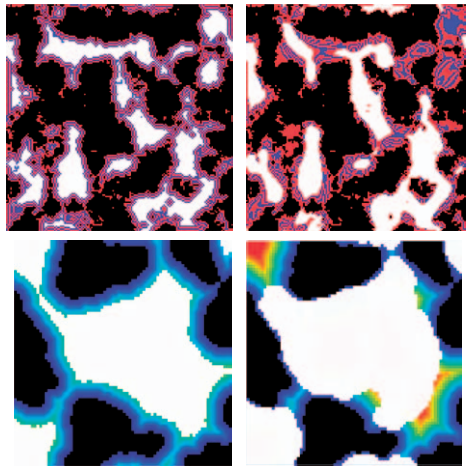

(a) (b)

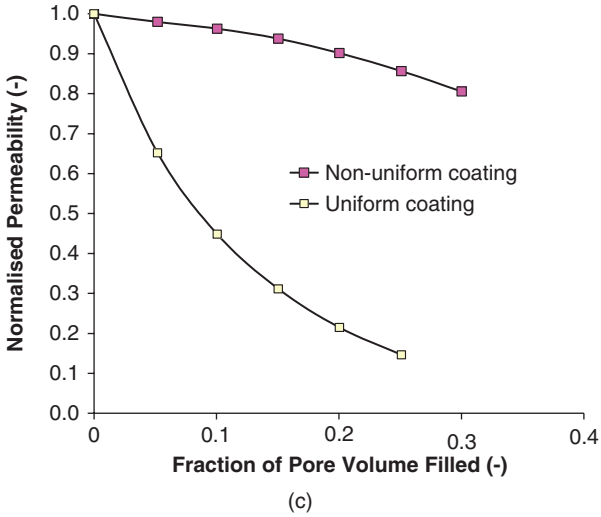

(c)

PLATE 7. Simulation of catalytic coating deposition at the same integral quantity of catalyst load. (a) Uniform coating and (b) non-uniform coating. The color code (blue to red) assists to visualize the local catalyst coating thickness from the filter surface. (c) Effect of coating distribution (uniform vs. non-uniform) on the DPF permeability (for Black and White version, see page 221).

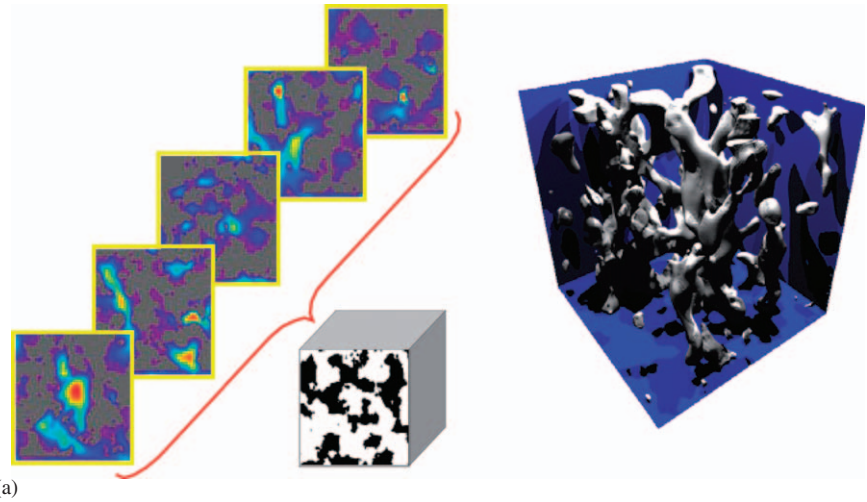

(a)

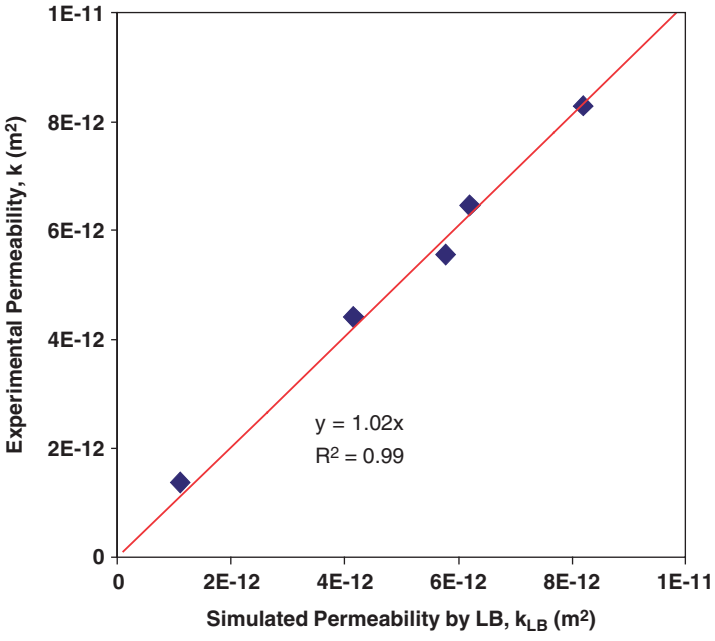

(b)

PLATE 8. (a) Velocity fields at different sections through the reconstructed filter wall (gray denotes the solid material, violet denotes lowest and red denotes highest velocity) and visualization of flow paths in the reconstructed filter wall and (b) comparison of experimental and simulated filter permeabilities (for Black and White version, see page 224).

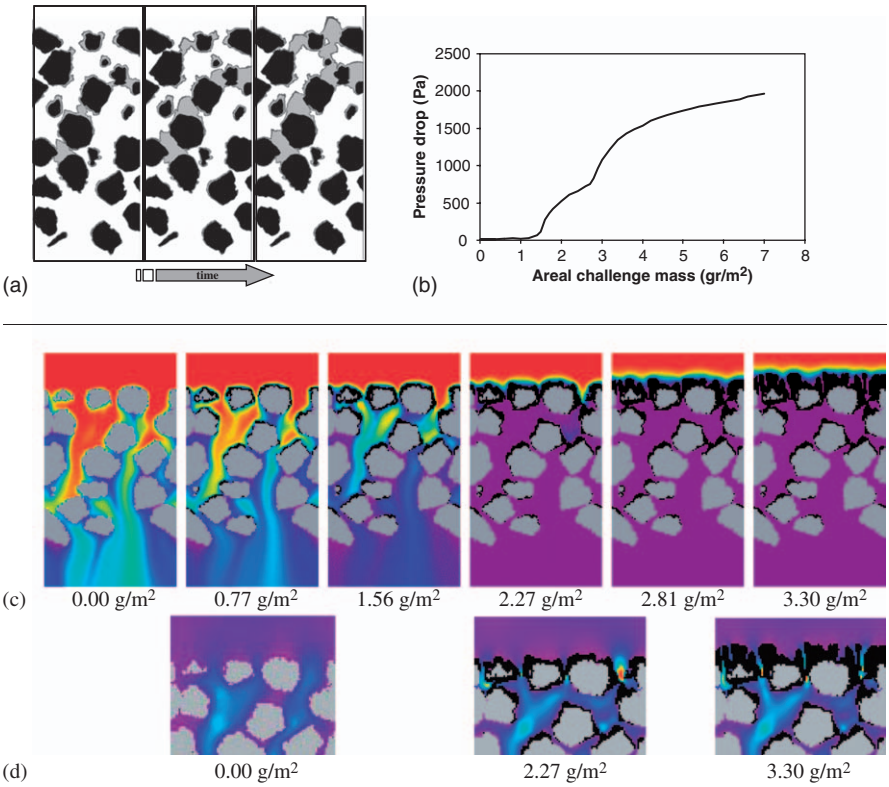

PLATE 9. Simulation of soot deposition on a filter wall. (a) Evolution of soot deposits (gray) in the wall (black is solid, white is pore space) and incipient cake formation; (b) pressure drop as function of challenge soot mass demonstrating the deep-bed to cake filtration transition; (c) visualization of soot deposition in an extruded ceramic (granular) filter wall and (d) development of soot deposits (black) and soot mass fraction in the wall (solid material is gray) to the onset of cake formation. Soot mass fraction scale is from 0 (violet) to the inflow value (red). In (d) the velocity on a section through the filter wall is shown, with overlay of the soot deposit shapes (for Black and White version, see page 235).

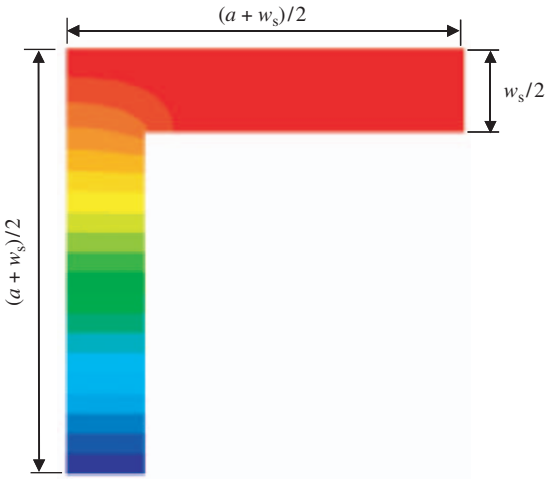

PLATE 10. Primary geometric unit for the effective conductivity of DPF (for Black and White version, see page 255).

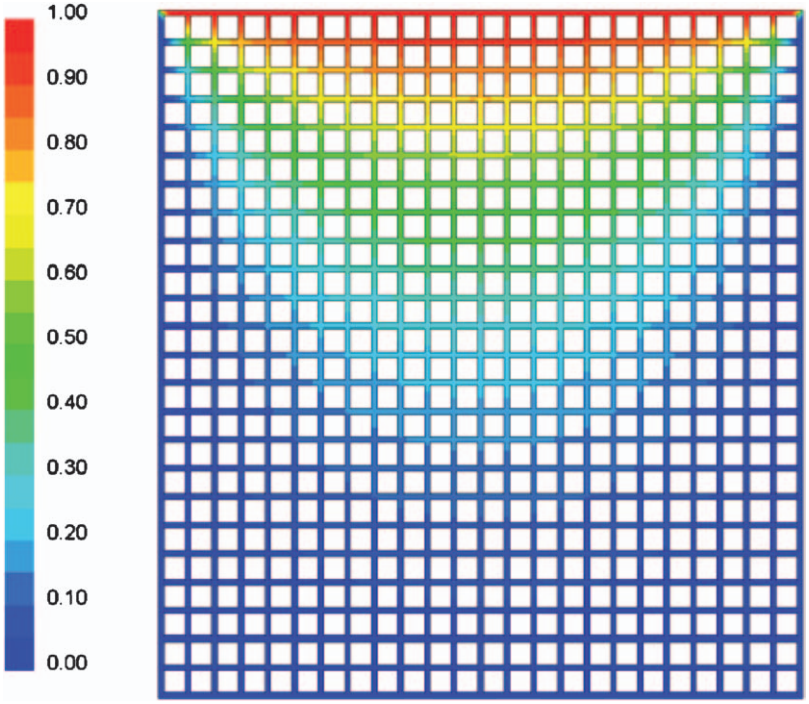

PLATE 11. Temperature distribution computed over a DPF segment with a unit temperature difference between the top and the other three sides (for Black and White version, see page 256).

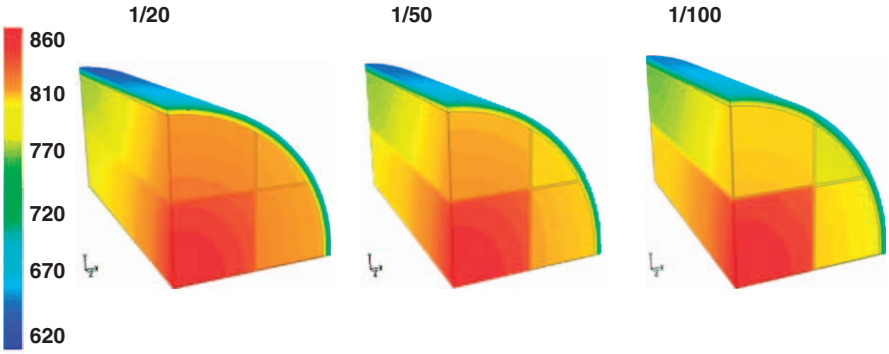

PLATE 12. Influence of the segment gluing material thermal conductivity to that of the segment (computed with the effective conductivity approach mentioned in the text) on the inter-segment heat transfer is shown (for Black and White version, see page 258).

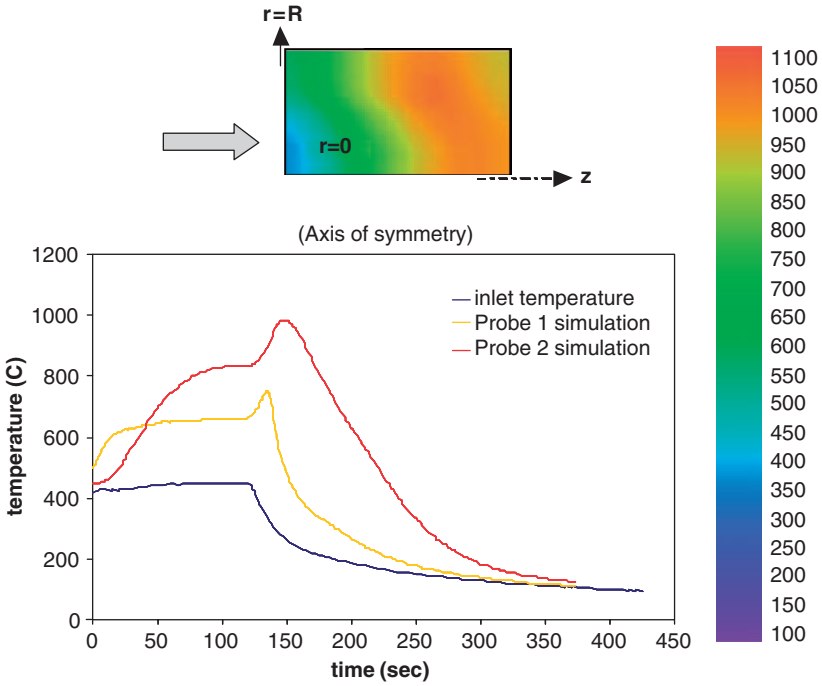

PLATE 13. Temporal evolution of temperature probes inserted in a regenerating DPF (bottom) along with the spatial distribution of filter temperature at 145 s, i.e. the moment of exothermic peak (top). Locations (r,z) in millimeter of temperature probes: Probe 1, (24.25,40) and Probe 2, (24.25,142) (for Black and White version, see page 259).

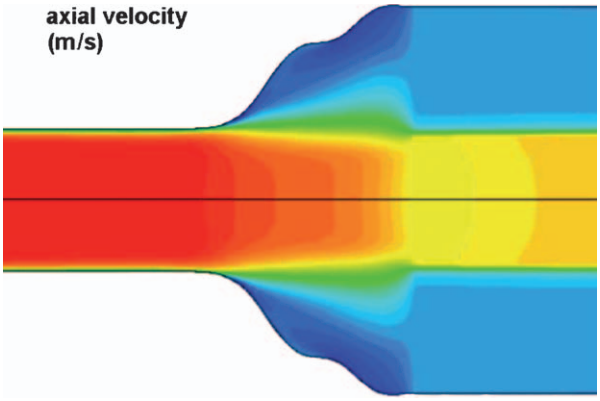

PLATE 14. Flow distribution at the entrance of a DPF with radially non-uniform soot distribution, resulting from incomplete regeneration (for Black and White version, see page 259).

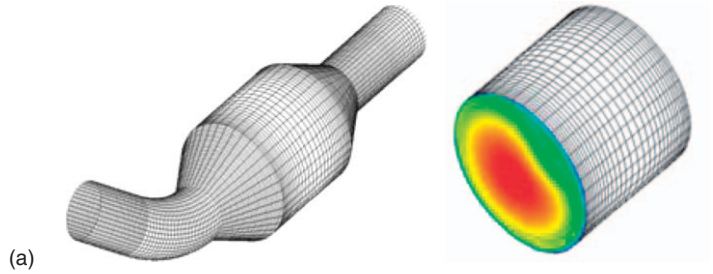

(a)

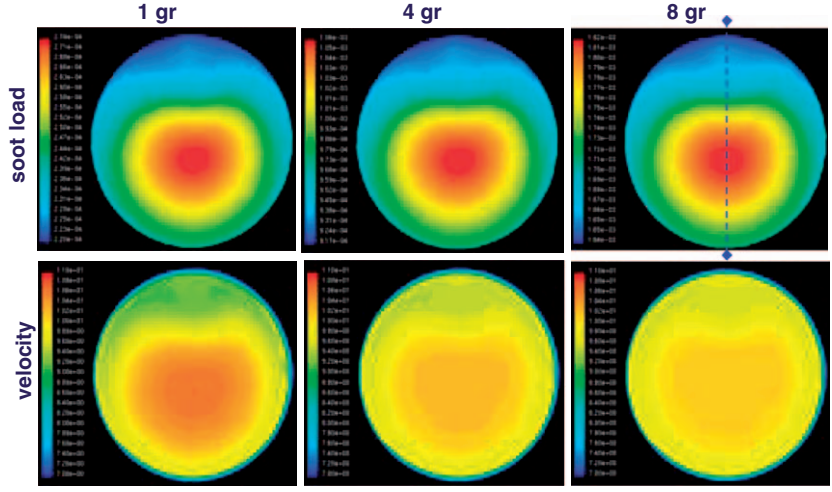

(b)

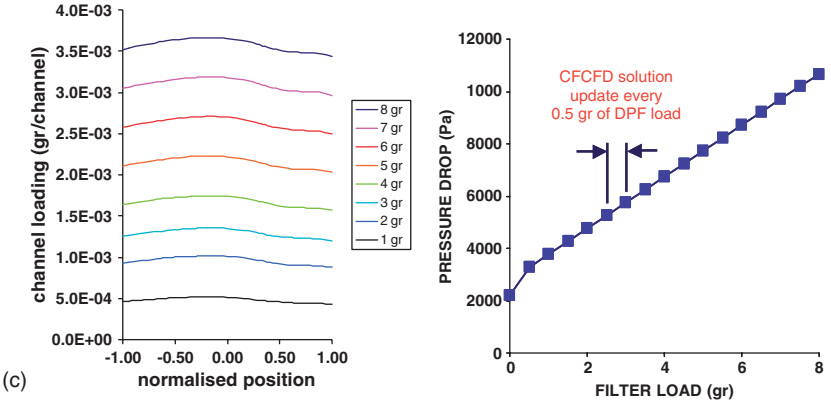

(c)

PLATE 15. (a) 3D simulation of a DPF placed downstream of a 45° bend in the exhaust. (b) Soot mass and velocity distribution at the inlet face at different soot loads of the filter. (c) Evolution of radial soot mass profile (along the dotted line) at different soot loads of the filter and resulting pressure drop (for Black and White version, see page 262).

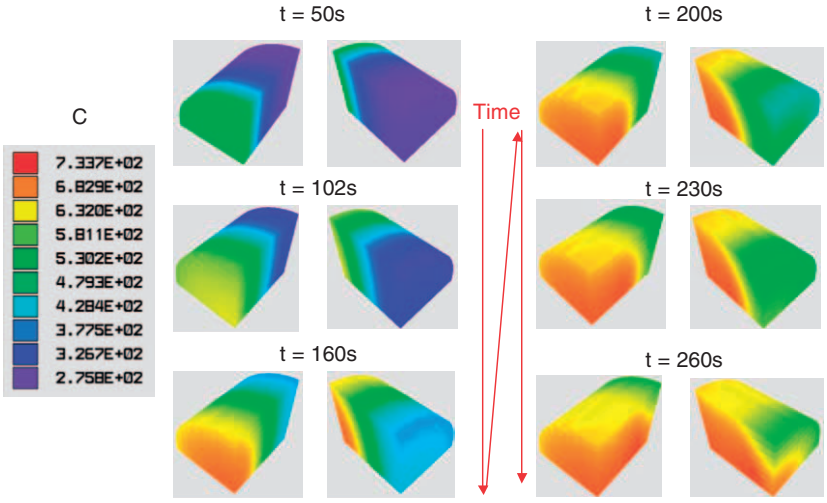

PLATE 16. 3D–DPF simulation. Example of temperature field evolution in a 11.25×12 in DPF during regeneration (for Black and White version, see page 263).

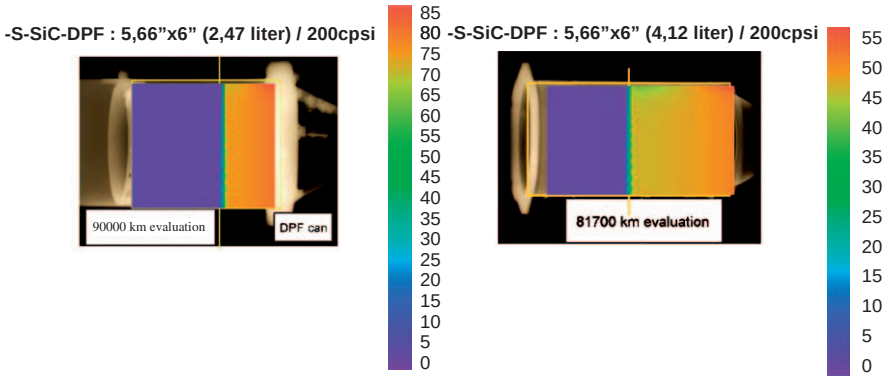

PLATE 17. Multichannel dynamic ash model. Simulation of additive ash accumulation at the end of the filter. Comparison with X-ray images of Blanchard *et al*. (2004) (for Black and White version, see page 264).